DOI: 10.1070/RCR4530

Crystals of the simple and complex nickel and cobalt sulfates as optical filters for the solar-blind technology

Vera L. Manomenova, Elena B. Rudneva, Alexey E. Voloshin

Shubnikov Institute of Crystallography, Russian Academy of Sciences
Leninsky prosp. 59, 119333 Moscow, Russian Federation

Published data on the design of UV optical filters for the solar-blind technology, a new trend in instrument making, are analyzed. The phase diagrams of the nickel sulfate and cobalt sulfate crystalline hydrates, the growth methods of the simple and complex nickel and cobalt sulfates and the results of studies on their structure and properties are considered. The dehydration mechanism and the factors influencing the thermal stability of the crystals are discussed. The problem of correct measurement of the dehydration temperature is addressed. Particular attention is paid to studies of correlations between the thermal stability and structural parameters of the crystals. Development trends of the title area are outlined.
The bibliography includes 119 references.

Contents

I. Introduction 585
II. The crystal of α-$NiSO_4 \cdot 6H_2O$ 586
III. Crystals of the nickel and cobalt families of double Tutton's salts 594
IV. Conclusion 605

I. Introduction

The energies of chemical bonds in most compounds, including the photoionization and photodissociation energies as well as the electronic excitation energies of atoms and molecules, fall in the ultraviolet (UV) and vacuum-UV regions. Yet another feature of the 200 – 300 nm wavelength range consists in that it is solar-blind due to absorption of solar radiation by the ozone layer (Fig. 1).

Utilization of this spectral region with certain kinds of devices and diagnostic equipment (provided full absorption in other subbands of the UV and visible regions) offers unique prospects for the design of a new class of highly sensitive devices for remote analysis and diagnosis.[1 – 4] The technology was termed 'solar-blind' and is being intensively developed in the USA, Israel, South Africa, United Kingdom, People's Republic of China and Russian Federation.

Main sources of natural noise in the visible and IR regions include solar radiation and thermal emission from various objects. Owing to intense absorption in the upper atmosphere, the intensity of solar radiation in the solar-blind region near the surface of the Earth is almost zero. It follows that the solar-blind spectral region is noise-free. Consequently, very high amplification factors can be

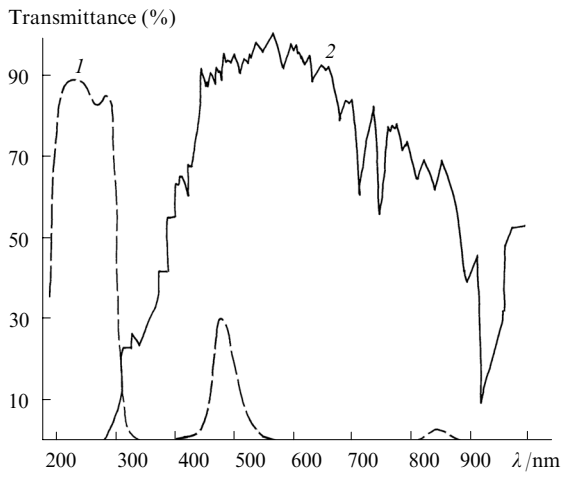


Figure 1. Transmission spectra of α-$NiSO_4 \cdot 6H_2O$ crystal (*1*) and solar light (*2*) in the 200 – 1000 nm wavelength region.

V.L.Manomenova. PhD, Chemistry, Senior Researcher of the Laboratory for Crystallization Processes at the IC RAS.
Telephhone: +7 (495) 330 – 8283, e-mail: manomenova@gmail.com
Current research interests: crystal growth from solutions.
E.B.Rudneva. PhD, Physics and Mathematics, Leading Researcher of the same Laboratory.
Telephone: +7 (495) 330 – 8283, e-mail: rudneva.lena@inbox.ru
Current research interests: crystal growth from solutions, X-ray topography.
A.E.Voloshin. Doctor of Physical and Mathematical Science, Deputy Director of the same Institute.
Telephone: +7 (495) 330 – 8283, e-mail: labsol@yandex.ru
Current research interests: X-ray topography, elementary steps of crystal growth.

Received 21 September 2015
Translation: A.M.Raevskiy

© 2016 Russian Academy of Sciences and Turpion Ltd.

obtained and extremely high sensitivity of remote analytical recording and photodetectors can be ensured.

Typically, solar-blind devices are used to monitor electric discharges and flames that are characterized by noticeable emission in the 250 – 280 nm spectral region. This specifies possible fields of application of such devices, *e.g.*, remote inspection of power transmission lines, analysis of contaminants in hydrocarbon raw materials and diagnosis of cancer. Besides, there are solar-blind-detector-based devices for tracking missile trajectories; this makes it possible to design active warfare protection systems as well as to protect nuclear reactors and hazardous production facilities from terrorist attacks.

Solar-blind detectors are made of various materials, *e.g.*, AlGaN, SiC, diamonds.[2, 3, 5 – 7] The spectral sensitivity does not go beyond the operating spectral region only for diamonds. However, tests of diamond detectors demonstrated that stable photoresponse is difficult to achieve because of (i) uncontrollable charge fluctuations in the bulk of the crystal and (ii) changes in the surface resistance of the crystal with time.[8] When using other types of photodetectors, a necessary component of a device is an efficient bandpass filter that is transparent in the 200 – 300 nm region and opaque in other spectral regions. It is band filtering that allows one to maintain a high signal-to-noise ratio and to obtain very high amplification factors (up to 10^8) in the UV region, thus ensuring a unique sensitivity of the equipment.

Earlier, glass filters were often used as UV filters. However, they are transparent in the 300 to 500 nm region, fully absorb radiation in the far UV region and exhibit a 'parasitic' transmission peak in the spectral region between 700 and 1500 nm. This reduces the efficiency of the glass light filters used in the solar-blind devices based on the detection of UV radiation in the 250 – 280 nm spectral region.

The crystal of α-$NiSO_4 \cdot 6H_2O$ was the first to be used as solar-blind UV optical filter.[9] However, low thermal stability and high hygroscopicity of the material gave an impetus for the search for other materials for solar-blind filters. As a result, two crystals with the desired properties were found, namely, $K_2Ni(SO_4)_2 \cdot 6H_2O$ and $(NH_4)_2Ni(SO_4)_2 \cdot 6H_2O$ (Refs 10 – 15). They belong to the nickel family of Tutton's salts $[M_2Ni(SO_4)_2 \cdot 6H_2O]$. The spectral characteristics of these crystals and α-$NiSO_4 \cdot 6H_2O$ crystal are rather close, but $K_2Ni(SO_4)_2 \cdot 6H_2O$ and $(NH_4)_2Ni(SO_4)_2 \cdot 6H_2O$ are characterized by higher dehydration temperatures and much lower hygroscopicity.

Operation of devices in the solar-blind spectral region, when illuminated by the sun of the neighbouring ranges, requires filtering of parasitic emission to a level of 10^{-15} and lower at a transmittance of 20% to 70% in the operating wavelength range. Exceptional requirements for the filtering are due to high limiting sensitivity of the detectors, *viz.*, 10^{-18} W cm^2 Hz$^{-1/2}$.

Special requirements are also imposed on the quality of crystals in connection with typical operating conditions of the devices that are widely used as components of aircraft equipment, namely, the temperature range from −65 to 85 °C as well as strong vibration and shock. Because of this particular attention should be paid to the quality of crystals, *viz.*, they should be crack-free, contain no large inclusions and be structurally and chemically stable in the specified temperature ranges.

Table 1. Positions of maxima in the absorption spectra of the crystals of simple and complex transition-metal sulfates and complex $[Co(H_2O)_6]^{2+}$ in the 250 – 1300 nm wavelength region.

Compound	Positions of absorption maxima /nm			Ref.
	UV radiation	visible light	IR radiation	
$CsTi(SO_4)_2 \cdot 12H_2O$	–	493	–	16
$CuSO_4 \cdot 5H_2O$	–	–	820	16
$CuSO_4 \cdot 6H_2O$	–	588	–	16
$CsV(SO_4)_2 \cdot 12H_2O$	391	562	–	16
$NH_4V(SO_4)_2 \cdot 12H_2O$	–	562	–	16
α-$NiSO_4 \cdot 6H_2O$	390	649, 714	1180	17
$(NH_4)_2Ni(SO_4)_2 \cdot 6H_2O$	392	633, 709	1124	17
$K_2Ni(SO_4)_2 \cdot 6H_2O$	385	643, 707	1120	10, 18
$Rb_2Ni(SO_4)_2 \cdot 6H_2O$	385	642, 708	–	18
$RbCr(SO_4)_2 \cdot 12H_2O$	–	707	–	16
$KCr(SO_4)_2 \cdot 12H_2O$	263	405, 571, 702	–	16
$NH_4Mn(SO_4)_2 \cdot 6H_2O$	–	476	–	16
$CsMn(SO_4)_2 \cdot 12H_2O$	–	476	–	16
$(NH_4)_2Fe(SO_4)_2 \cdot 6H_2O$	–	–	970, 1190	16
$[Co(H_2O)_6]^{2+}$	340	520	1230	16

It is necessary that solar-blind optical filters have high transmittance in the 250 – 280 nm wavelength region and deep absorption beyond it. The data in Table 1 show that, among the simple and complex transition-metal sulfates, such crystals as α-$NiSO_4 \cdot 6H_2O$, $K_2Ni(SO_4)_2 \cdot 6H_2O$ and $(NH_4)_2Ni(SO_4)_2 \cdot 6H_2O$, $Rb_2Ni(SO_4)_2 \cdot 6H_2O$ and $Cs_2Ni(SO_4)_2 \cdot 6H_2O$ seem to be the most promising for fabrication of solar-blind filters. These crystals are transparent in the 200 – 300 nm region and have absorption bands in the UV, visible and near-IR regions. Also, of considerable interest is the $K_2Co(SO_4)_2 \cdot 6H_2O$ crystal belonging to the cobalt family of Tutton's salts $[M_2Co(SO_4)_2 \cdot 6H_2O]$, because the octahedral complex $[Co(H_2O)_6]^{2+}$ also exhibits the necessary spectral characteristics (see Table 1).

This review is concerned with specific features of crystallization of the simple and complex nickel and cobalt sulfates, with the influence of growth conditions on the crystal structure and optical properties as well as with correlations between the thermal stability and structure of the crystals belonging to the nickel and cobalt families of Tutton's salts.

II. The crystal of α-$NiSO_4 \cdot 6H_2O$

II.1. The phase diagram of the $NiSO_4 - H_2O$ system: an analysis

The first detailed study[19] of the $NiSO_4 - H_2O$ system in the temperature interval between −5 and 110 °C at atmospheric pressure revealed four stable and four metastable solid phases representing eight different nickel sulfate hydrates. The transition temperatures and the equilibrium phases are listed in Table 2 and the solubility curve of $NiSO_4$ in water[19] is shown in Fig. 2. Later on,[20, 21] the transition temperatures were refined, namely, the temperature of the $NiSO_4 \cdot 7H_2O \rightarrow \alpha$-$NiSO_4 \cdot 6H_2O$ transition (point *F*) is 31.5 °C while that of the α-$NiSO_4 \cdot 6H_2O \rightarrow$ β-$NiSO_4 \cdot 6H_2O$ transition (point *G*) is 53.3 °C. It follows

Table 2. Phase transitions in the $NiSO_4-H_2O$ system.[19]

Point in the phase diagram (Fig. 2)	Equilibrium solid phases	Type of equilibrium	Transition temperature /°C	c_{NiSO4} /g per 100 g H_2O
E	Ice – $NiSO_4 \cdot 7H_2O$	Stable	−3.15	26.3
F	$NiSO_4 \cdot 7H_2O$ – α-$NiSO_4 \cdot 6H_2O$	"	29.1	43.7
G	α-$NiSO_4 \cdot 6H_2O$ – β-$NiSO_4 \cdot 6H_2O$	"	60.3	57.0
L	β-$NiSO_4 \cdot 6H_2O$ – $NiSO_4 \cdot 5H_2O$	Metastable	98	79.3
K	β-$NiSO_4 \cdot 6H_2O$ – $NiSO_4 \cdot 4H_2O$	"	97.2	78.5
J	β-$NiSO_4 \cdot 6H_2O$ – $NiSO_4 \cdot 3H_2O$	"	96.4	78.0
I	β-$NiSO_4 \cdot 6H_2O$ – $NiSO_4 \cdot 2H_2O$	"	90.3	73.1
H	β-$NiSO_4 \cdot 6H_2O$ – $NiSO_4 \cdot H_2O$	Stable	84.8	69.0

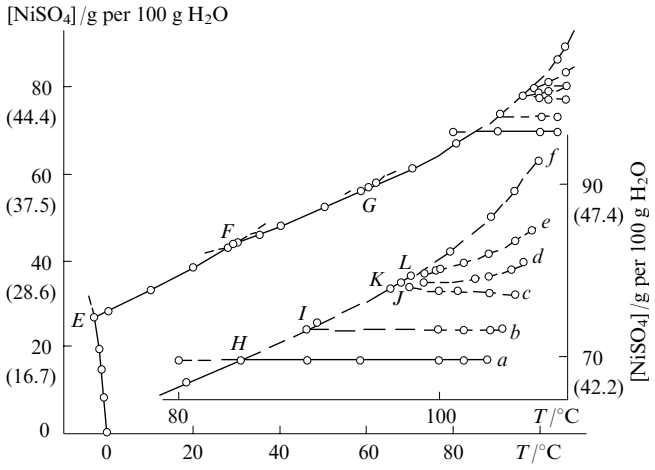


Figure 2. The solubility curve of $NiSO_4$ in water (see Table 2).[19] Solid and dashed lines correspond to the stable and metastable phases, respectively.
Phases: α-$NiSO_4 \cdot 6H_2O$ (*FG*), β-$NiSO_4 \cdot 6H_2O$ (*Lf*), $NiSO_4 \cdot 7H_2O$ (*EF*), $NiSO_4$ (*Ha*), $NiSO_4 \cdot 2H_2O$ (*Ib*), $NiSO_4 \cdot 3H_2O$ (*Jc*), $NiSO_4 \cdot 4H_2O$ (*Kd*) and $NiSO_4 \cdot 5H_2O$ (*Le*).
Here and in Fig. 3 the numbers in parentheses denote the content of a particular component in mass %.

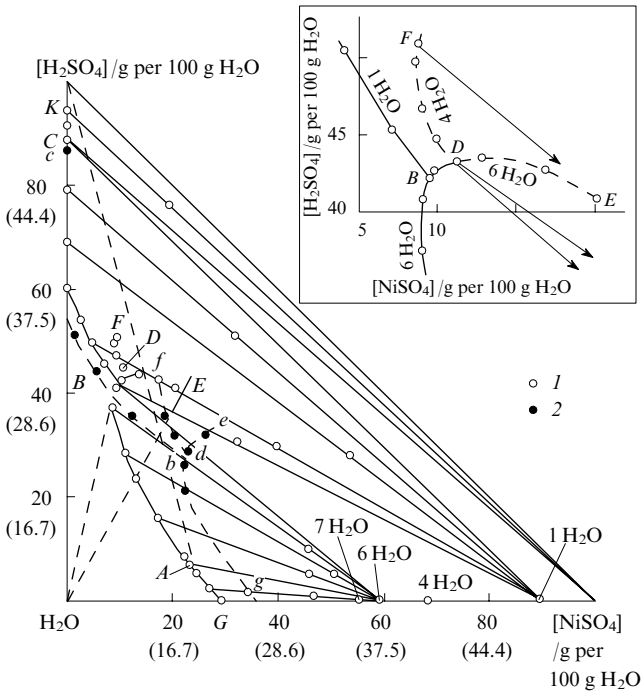


Figure 3. Solubility isotherms of the $NiSO_4-H_2SO_4-H_2O$ system at 25 (*1*) and 50 °C (*2*).[22]

that stable growth of α-$NiSO_4 \cdot 6H_2O$ crystals from aqueous nickel sulfate solutions is possible in the temperature interval from 31.5 to 53.3 °C.

II.2. The phase diagram of the $NiSO_4-H_2SO_4-H_2O$ system: an analysis

The solubility phase diagram of the ternary system $NiSO_4-H_2SO_4-H_2O$ was studied by different authors in the temperature range from 0 to 90 °C.[22–24] The first solubility isotherms of this system were obtained[22] at 25 and 50 °C (see Fig. 3).

The 25 °C solubility isotherm consists of six solubility curves. Four of them correspond to stable equilibria and two correspond to metastable ones. At 25 °C, the stable solid phases $NiSO_4 \cdot 7H_2O$, $NiSO_4 \cdot 6H_2O$, $NiSO_4 \cdot H_2O$ and $NiSO_4$ correspond to the *GA*, *AB*, *BC* and *CK* branches of the phase diagram, respectively. The existence range of the metastable phase $NiSO_4 \cdot 4H_2O$ corresponds to the *DF* curve, while the metastable phase $NiSO_4 \cdot 6H_2O$ corresponds to the *BE* branch (continuation of the *AB* curve, see inset in Fig. 3).

The solubility of nickel sulfate is maximum in the absence of sulfuric acid (existence range of $NiSO_4 \cdot 7H_2O$) and abruptly decreases as H_2SO_4 is added to the solution, being at most a few fractions of a percent at high concentrations of sulfuric acid (> 70 mass %).

At 50 °C, the $NiSO_4 \cdot 7H_2O$ phase disappears and the solubility curve of nickel sulfate hexahydrate now begins at point *A* that corresponds to an aqueous solution containing no sulfuric acid. As at 25 °C, the solubility of nickel sulfate at this point is maximum. In all other respects, the solubility isotherms of the $NiSO_4-H_2SO_4-H_2O$ system at 25 and 50 °C obey a similar pattern, except for the increase in the solubilities of all the existing crystalline phases with increasing temperature. At 90 °C, only two stable solid phases, *viz.*, $NiSO_4 \cdot H_2O$ and $NiSO_4$, were found in the ternary system in question.[22]

The solubility isotherms of the $NiSO_4-H_2SO_4-H_2O$ system were also studied at 0, 20, 40 and 80 °C.[23] The compositions of the saturated solutions that are in equilibrium with the solid phases existing at these temperatures

are shown in the corresponding isothermal sections of the phase diagram of this system (Figs ES.1 – ES.4).†

More recently, the ternary system $NiSO_4 - H_2SO_4 - H_2O$ was studied again at 0 and 25 °C by other authors. Two equilibrium solid phases, $NiSO_4 \cdot H_2O$ and $H_2SO_4 \cdot H_2O$, were found at 0 °C.[24] They were not reported previously.[23] This can be explained by the fact that the range of the liquid phase compositions studied [23] was incomplete and limited to a sulfuric acid content of 50.92 mass %, whereas nickel sulfate monohydrate and sulfuric acid monohydrate were revealed at H_2SO_4 concentrations higher than 52.88 mass %.[24] In all other respects, the data on the solubility at 0 °C obtained in Refs 23 and 24 are in reasonable agreement.

At 25 °C, the existing ranges of the stable phases $NiSO_4 \cdot 7H_2O$, $NiSO_4 \cdot 6H_2O$, $NiSO_4 \cdot H_2O$ and $NiSO_4$ and the transition points [24] are consistent with the results reported by Babajewa and Daniluschkina.[23] However, Addlestone [24] restricted himself to the detection of the metastable phase $NiSO_4 \cdot 4H_2O$ at sulfuric acid concentrations of ~45 mass % – 50 mass% and did not investigate the corresponding branch of the solubility curve in detail.

The stable and metastable phases found in the $NiSO_4 - H_2SO_4 - H_2O$ system in the temperature range from 0 to 90 °C are listed in Table 3.

A comparison of the data presented in Tables 2 and 3 and in Figs ES.1 – ES.4 suggests that the addition of sulfuric acid to the $NiSO_4 - H_2O$ system causes the following changes:

— abrupt decrease in the solubilities of the nickel sulfates existing at particular temperatures with increasing acid concentration;

— formation of new stable crystalline phases, namely, $NiSO_4 \cdot 2H_2O$, $NiSO_4 \cdot H_2O$ and $NiSO_4$; a decrease in the number of water molecules in the nickel sulfate hydrates with increasing sulfuric acid concentration;

— extension of the crystallization range of α-$NiSO_4 \cdot 6H_2O$ owing to a shift of the lower temperature boundary of the existence range of this phase from 31.5 to 0 °C.

Unfortunately, the polymorphic forms of solid $NiSO_4 \cdot 6H_2O$ were determined fragmentarily.[22, 24] The existence ranges of the stable α- and β-forms of $NiSO_4 \cdot 6H_2O$ were reported,[23] but a wide temperature interval from 40 to 80 °C in the phase diagram of the $NiSO_4 - H_2SO_4 - H_2O$ system was not studied. Consequently, the possibility for the crystallization range of α-$NiSO_4 \cdot 6H_2O$ to extend owing to a shift of the upper temperature boundary of the existence range of this phase towards $T > 53.3$ °C remained unclear.

Table 3. Solid phases that form in the $NiSO_4 - H_2SO_4 - H_2O$ system in the temperature interval from 0 to 90 °C.

T /°C	Solid phases		Ref.
	stable	metastable	
0	$NiSO_4 \cdot 7H_2O$, α-$NiSO_4 \cdot 6H_2O$	–	23
	$NiSO_4 \cdot 7H_2O$, $NiSO_4 \cdot 6H_2O$, $NiSO_4 \cdot H_2O$, $H_2SO_4 \cdot H_2O$	–	24
20	$NiSO_4 \cdot 7H_2O$, α-$NiSO_4 \cdot 6H_2O$, $NiSO_4 \cdot 2H_2O$	–	23
25	$NiSO_4 \cdot 7H_2O$, $NiSO_4 \cdot 6H_2O$, $NiSO_4 \cdot H_2O$, $NiSO_4$	$NiSO_4 \cdot 4H_2O$	22
	$NiSO_4 \cdot 7H_2O$, $NiSO_4 \cdot 6H_2O$, $NiSO_4 \cdot H_2O$, $NiSO_4$	$NiSO_4 \cdot 4H_2O$	24
40	α-$NiSO_4 \cdot 6H_2O$, $NiSO_4 \cdot 2H_2O$	$NiSO_4 \cdot 5H_2O$, $NiSO_4 \cdot 4H_2O$	23
50	$NiSO_4 \cdot 6H_2O$, $NiSO_4 \cdot H_2O$, $NiSO_4$	$NiSO_4 \cdot 4H_2O$	22
80	β-$NiSO_4 \cdot 6H_2O$, $NiSO_4 \cdot 2H_2O$	–	23
90	$NiSO_4 \cdot H_2O$, $NiSO_4$	–	23

† For Figs ES.1. – ES.38., see the Electronic Supplement to this review, http://www.iopscience.org/rcr.

II.3. The habit and the crystal structure of α-$NiSO_4 \cdot 6H_2O$

Emerald green α-$NiSO_4 \cdot 6H_2O$ crystals belong to the tetragonal crystal system (tetragonal-trapezohedral symmetry class 422, space group $P4_12_12$). The unit cell parameters are as follows: $a = 6.783$ Å, $c = 18.288$ Å, $V = 841.4(3)$ Å^3, $Z = 4$, $\rho = 2.075$ g cm^{-3} (Refs 25 – 28). The crystal habit of α-$NiSO_4 \cdot 6H_2O$ is shown in Fig. ES.5.

Crystal α-$NiSO_4 \cdot 6H_2O$ has a layered structure, the layers being comprised of slightly distorted $[Ni(H_2O)_6]^{2+}$ octahedra and $[SO_4]^{2-}$ tetrahedra and stacked perpendicular to the c axis. Each $[Ni(H_2O)_6]^{2+}$ octahedron is linked through a network of hydrogen bonds to (i) four sulfate groups that lie in the same (001) plane (this is also the cleavage plane, see Fig. 4 *a*) and (ii) two $[SO_4]^{2-}$ tetrahedra in the upper and lower layers. The bonds between the Ni octahedron and sulfate groups lying in the (001) plane correspond to four shortest distances Ni – S.[28]

The O(1), O(2) and O(3) atoms belong to water molecules, while the O(4) and O(5) atoms belong to sulfate groups. The O(2) and O(3) atoms are each connected through two hydrogen bonds to the O(4) and O(5) atoms which act as electron density acceptors. For the O(1) atom, the acceptors are the O(5) atom and the O(3) atom of water molecule from the neighbouring coordination polyhedron. Thus, the structure of α-$NiSO_4 \cdot 6H_2O$ comprises layers of $[Ni(H_2O)_6]^{2+}$ and $[SO_4]^{2-}$ groups connected not only by a network of hydrogen bonds within a layer, but also by hydrogen bonds between the layers, the inter-layer hydrogen bonds being as strong as the in-layer ones.[27, 29]

The layers are stacked in such a manner that the $[Ni(H_2O)_6]^{+}$ coordination polyhedra are grouped around the 4_1 axes, the sulfate groups in the next layer being almost exactly above them along the [001] direction; such an alternation occurs with an increment of $c/2$ (see Fig. 4 *b*). The O(1) and O(3) atoms of water molecules form right-hand helical structures along the 4_1 axes. It is believed [27] that these helices make the major contribution to the optical activity of α-$NiSO_4 \cdot 6H_2O$ crystals. In the crystal structure of α-$NiSO_4 \cdot 6H_2O$, the $[SO_4]^{2-}$ tetrahedron is the least distorted among the known structures of transition metal sulfates.[28]

The crystal structures of two polymorphic forms, namely, tetragonal α-$NiSO_4 \cdot 6H_2O$ and monoclinic β-$NiSO_4 \cdot 6H_2O$ (space group $C2/c$, $Z = 8$), were compared to explain different stabilities of these phases.[30] The β-form undergoes a spontaneous transformation to the tetragonal α-form at $T \geqslant 35$ °C.[31] It was found that the lower stability of the former is due to the absence of chemical bonds between the nickel polyhedra of the neighbouring layers [*cf.* the O(1) – O(3) bonds in α-$NiSO_4 \cdot 6H_2O$]. In

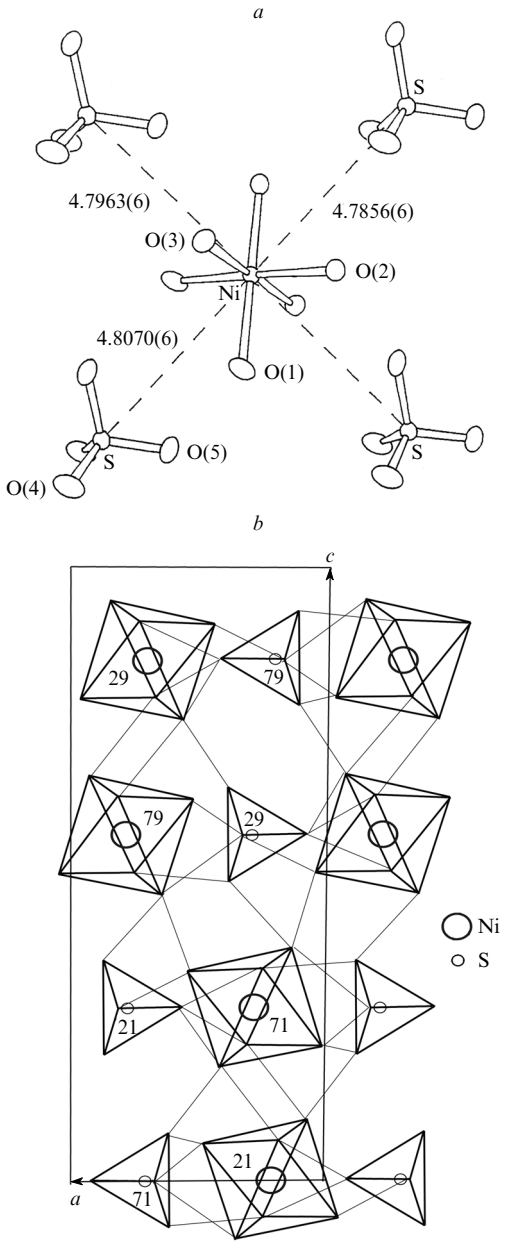


Figure 4. Crystal structure of α-$NiSO_4 \cdot 6\,H_2O$.[27]
Sulfate groups surrounding the nickel octahedron within the same layer in the (001) plane (*a*),[28] projection of $[Ni(H_2O)_6]^{2+}$ and $[SO_4]^{2-}$ polyhedra on the (010) plane (*b*); the numbers denote the distances of nickel and sulfur atoms from the *b* plane (in 1/100*b*).

β-$NiSO_4 \cdot 6\,H_2O$, water molecules of the nickel octahedron form ten hydrogen bonds with sulfate groups.[30]

II.4. Optical properties of α-$NiSO_4 \cdot 6\,H_2O$ crystal

The α-$NiSO_4 \cdot 6\,H_2O$ crystal is an optically uniaxial negative one. The ordinary and extraordinary refractive indices (n_o and n_e, respectively) at different wavelengths of transmitted light are listed in Table 4. Dispersion of the ordinary refractive index and birefringence is illustrated in Fig. ES.6.[33]

The absorption spectra, circular dichroism and optical activity of α-$NiSO_4 \cdot 6\,H_2O$ crystals have been studied in detail.[27, 33 – 36] The band absorption spectrum in the 200 – 1100 nm wavelength range is determined by the presence of the $[Ni(H_2O)_6]^{2+}$ octahedron in the crystal structure.[27, 34, 37] A free divalent nickel ion in an octahedral environment has two unpaired electrons. From the energy level diagram of a d^8-ion in octahedral field, it follows that four spin-allowed transitions can occur, corresponding to four absorption bands of the nickel ion surrounded by six water molecules (Fig. ES.7).[37]

Table 5 presents the theoretical and experimental absorption frequencies of α-$NiSO_4 \cdot 6\,H_2O$ crystal and corresponding transitions.

Table 4. Refractive indices of α-$NiSO_4 \cdot 6\,H_2O$ crystal at different wavelengths of transmitted light.[32]

λ /nm	n_o	n_e
658.3	1.5078	1.4844
689	1.5109	1.4873
486.2	1.5173	1.4930

Table 5. Absorption frequencies of α-$NiSO_4 \cdot 6\,H_2O$ crystal and corresponding transitions.[33, 34]

Transition	Frequency /cm^{-1}		
	calculations	experiment [a]	
$^3A_{2g} \rightarrow {}^3T_{2g}$	8500	8500 (1176)	8695 (1150)
$^3A_{2g} \rightarrow {}^1E_g(D)$	13900	14120 (708)	14005 (714)
$^3A_{2g} \rightarrow {}^3T_{1g}(F)$	14150	15300 (654)	15408 (649)
$^3A_{2g} \rightarrow {}^3T_{1g}(P)$	25150	25900 (386)	25000 (400)

Note. The frequencies in the second and third columns were taken from Ref. 34, those in the fourth column were taken from Ref. 33. [a] Numbers in parentheses denote the corresponding λ values (in nm).

The α-$NiSO_4 \cdot 6\,H_2O$ crystal exhibits circular dichroism ($\Delta\varepsilon$), *i.e.*, it differently absorbs right-hand and left-hand circularly polarized light.[38]

$$\Delta\varepsilon = (\varepsilon_L - \varepsilon_R) \quad (1)$$

Absorption maxima and circular dichroism correspond to the same wavelength if they are related to the same transition. The absorption spectra of polarized light measured parallel to the optical axis and the circular dichroism spectrum of polarized light measured perpendicular to the optical axis of the crystal are shown in Fig. ES.8.[34]

A circular dichroism study [33] carried out parallel and perpendicular to the optical axis revealed that in the latter case the effect was 4.4 times weaker than in the former.

The results of optical rotatory dispersion studies of α-$NiSO_4 \cdot 6\,H_2O$ crystal were reported.[27, 32 – 35] Figure ES.9 presents the optical rotatory dispersion measured parallel to the optical axis of the crystal.[33]

II.5. Dehydration studies of α-$NiSO_4 \cdot 6\,H_2O$ crystal

In the crystal structure, water molecules are linked to anions and cations through weak hydrogen bonds; therefore, such crystals are unstable and readily lose water on heating. Processes accompanying dehydration of α-$NiSO_4 \cdot 6\,H_2O$ crystals were studied.[39 – 45] These processes are thermody-

namically nonequilibrium and depend strongly on the experimental conditions.

Investigations of morphological and structural features of transformations occurring in the course of thermal decomposition of α-$NiSO_4 \cdot 6\,H_2O$ are of considerable interest for basic research and practice because this offers prospects for controlling the dehydration of these crystals by varying external conditions.

Information on particular steps of structural transformations occurring on heating of α-$NiSO_4 \cdot 6\,H_2O$ is contradictory. For instance, crystalline samples placed in (i) closed sample pans and (ii) pans with pin holes for gas exchange with the environment were studied by differential scanning calorimetry (DSC) and thermogravimetric analysis (TGA) in the temperature interval from 25 to 300 °C.[39,40] The heating rate was 10 °C min^{-1} in Ref. 40 and not specified in Ref. 39. It was found that the crystals in the closed pans lose only two bound water molecules in this temperature range

$$\alpha\text{-}NiSO_4 \cdot 6\,H_2O\ (solid) \longrightarrow \longrightarrow NiSO_4 \cdot 4\,H_2O\ (solid) + 2\,H_2O\ (liquid) \quad (2)$$

In the experiments with pin-holed pans, bound water could evaporate and thus leave the system, so the first step of the dehydration of α-$NiSO_4 \cdot 6\,H_2O$ crystals involving the loss of two water molecules was followed by the loss of two more water molecules [39,40]

$$NiSO_4 \cdot 4\,H_2O\ (solid) \longrightarrow NiSO_4 \cdot H_2O\ (solid) + 3\,H_2O\ (gas) \quad (3)$$

$$NiSO_4 \cdot H_2O\ (solid) \longrightarrow NiSO_4\ (solid) + H_2O\ (gas) \quad (4)$$

Thus, the water vapour above the crystal surface retards thermal decomposition of the crystal.

Thermogravimetric studies [41] were carried out using single-crystal, powdered (particle diameter was 100 μm) and granulated α-$NiSO_4 \cdot 6\,H_2O$ samples. Granules were prepared by pressing the powder at high pressure. The samples were heated at a rate of 5 °C min^{-1} in the temperature range from 30 to 450 °C. The results obtained were used to plot the rate of change in mass *vs.* temperature (differential thermogravimetry, DTG). No phase analysis of reaction products was performed, the composition of the atmosphere was not specified and the type of the system under study (closed or open) is unknown.

According to TGA results obtained on heating powdered and granulated α-$NiSO_4 \cdot 6\,H_2O$, the DTG curves demonstrate three clearly seen minima at 134, 178 and 345 °C, corresponding to stepwise loss of two, three and one water molecules from the crystal structure. An analysis of the DTG curves for the single-crystal samples of α-$NiSO_4 \cdot 6\,H_2O$ revealed four consecutive phase transitions at 129, 187, 214 and 390 °C; this was interpreted as sequential loss of one, two, two and one more bound water molecule.[41]

It should be noted that four endothermic peaks were also observed in other studies.[39,40] Since in both cases the experimental setups were equipped with gas analyzers, one of these peaks was interpreted with certainty as a result of evaporation of water eliminated during the first step of dehydration. In Ref. 41, the composition of the vapour phase was not analyzed. Because of this, the results [39,40] seem to be more reliable.

More recently,[45] the influence of heating rate, pressure and mass of crystalline powder on the order of dehydration steps was investigated in the temperature interval from 300 to 750 K; the results obtained are presented in Fig. 5.

As can be seen, the pattern of the TGA and differential thermal analysis (DTA) curves varies greatly depending on the experimental conditions. During heating of 30-mg powdered α-$NiSO_4 \cdot 6\,H_2O$ samples at a rate of 8 °C min^{-1} in air at normal pressure, three consecutive phase transitions corresponding to the loss of two, three and one water molecules are observed (see Fig. 5 *a*). By and large, this agrees with the data cited above [39,40] and with the results obtained for single-crystalline powder.[41] However, the mass loss corresponding to the first endothermic DTA peak increased as the mass of the sample and the heating rate decreased (see Fig. 5 *b*). It was emphasized that similar changes were also observed as the particle size decreased. Reduction of the external pressure led to the formation of $NiSO_4 \cdot H_2O$ in the first dehydration step (see Fig. 5 *c*).[45]

Attempts to find correlations between the dehydration patches on the crystal surface (a new phase formed on them) and dislocation outcrops were reported.[42–44] Experiments using fresh (001) cleavages of single-crystal α-$NiSO_4 \cdot 6\,H_2O$ samples were carried out *in vacuo* both isothermally and

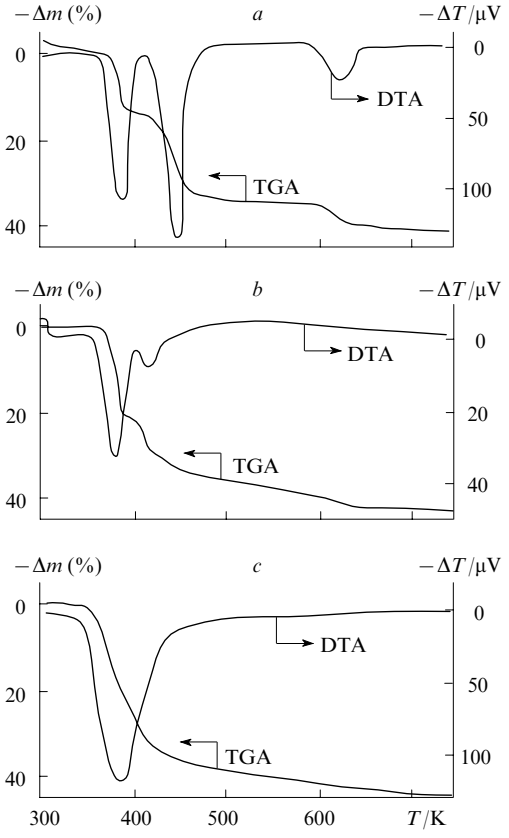


Figure 5. DTA and TGA curves of α-$NiSO_4 \cdot 6\,H_2O$ obtained in different experimental conditions.[45]
Notations: m_0 is the mass of the sample and ϕ is the heating rate of the sample.
Conditions: m_0 = 30 mg, ϕ = 8 °C min^{-1} in air (*a*); m_0 = 10 mg, ϕ = 4 °C min^{-1} in N_2 atmosphere (*b*) and m_0 = 30 mg, ϕ = 8 °C min^{-1} at a reduced pressure of 1.5×10^{-2} Pa (*c*).

dynamically (on heating at a rate of 1.72 °C min^{-1}) in the temperature interval from 20 to 220 °C.

It was found[43] that dehydration patches on the (001) plane do not emerge at random, *viz*., they are preferentially formed on isolated and aligned dislocations (Fig. ES.10 *a*). In the initial steps of thermal decomposition of α-$NiSO_4 \cdot 6H_2O$, the number of dehydration patches remains constant (Fig. ES.10 *b*) and the process develops through extension of the patches. The kinetics of isothermal dehydration of single-crystalline and powdered α-$NiSO_4 \cdot 6H_2O$ samples were studied[44] by vacuum TGA and optical microscopy. It was found that the dehydration rate depends on the density of dislocations outcropping on the surface (Fig. ES.11).

Preferential nucleation of the new phase at dislocation outcrops was explained by reduced free energy of nucleation at those sites.[43]

Interestingly, experiments[43] with single-crystalline α-$NiSO_4 \cdot 6H_2O$ samples carried out isothermally *in vacuo* ($P \leqslant 1.33 \cdot 10^{-4}$ Pa) in the temperature range from 35 to 50 °C resulted in the monohydrate

$$\alpha\text{-}NiSO_4 \cdot 6H_2O\ (\text{solid}) \longrightarrow NiSO_4 \cdot H_2O\ (\text{solid}) + 5H_2O\ (\text{gas}) \quad (5)$$

The influence of the duration of isothermal dehydration on the decomposition degree (ζ) of the crystalline material was studied (Fig. ES.12).[44] The activation energies (E_a) of dehydration of powdered and single-crystalline samples ($E_a \approx 15 \pm 2$ and $\approx 16 \pm 2$ kcal mol^{-1}, respectively) were evaluated[44] using linear portions of the $\zeta = f(t)$ plots (see Fig. ES.11). The results obtained were confirmed by optical microscopy, namely, the tangential growth rates of nuclei of the new phase (dehydration patches) on the (001) face of the single-crystalline sample were studied. The plots of the size of dehydration patches (D) *vs*. time (t) were strictly linear above 40 °C and showed noticeable curvature at lower temperatures (Fig. ES.13). The average activation energy of nucleation calculated from the Arrhenius equation for the linear portions of the plots was $\sim 20 \pm 4$ kcal mol^{-1} (Ref. 44).

Re-construction of the $\zeta = f(t)$ plot for single-crystalline samples in the coordinates $[-\ln(1-\zeta)]^{1/2} = f(t)$ gives a straight line at $0.001 < \zeta < 0.96$ (Fig. ES.14). From the results obtained, it was concluded[44,45] that isothermal dehydration on the crystal surface accompanied by nucleation obeying a power law is described by the Avrami – Erofeev equation[46]

$$\zeta = 1 - \exp[-(kt)^p] \quad (6)$$

where the kinetic exponent is $p = 2$ and k is the rate constant for decomposition.

The kinetics of non-isothermal dehydration and morphology changes on the surface and in the inner layers of α-$NiSO_4 \cdot 6H_2O$ samples were investigated in detail by IR spectroscopy, X-ray powder diffractometry and optical microscopy.[45] It was established that non-isothermal dehydration involves three steps.

Step I. The formation of a liquid phase (supersaturated aqueous $NiSO_4 \cdot 4H_2O$ solution) on the surface of α-$NiSO_4 \cdot 6H_2O$ and nucleation of $NiSO_4 \cdot 4H_2O$ crystals. At $\zeta \geqslant 0.15$, the entire surface is covered with $NiSO_4 \cdot 4H_2O$ and subsequent dehydration proceeds through advancement of the reaction surface inwards. The process is accompanied by subsequent dehydration of the outer layer of $NiSO_4 \cdot 4H_2O$ to give dihydrate; this makes it difficult for the water vapour evolved in the interior as a result of the phase transition

$$\alpha\text{-}NiSO_4 \cdot 6H_2O \rightleftharpoons NiSO_4 \cdot 4H_2O + 2H_2O\ (\text{gas}) \quad (7)$$

to escape through diffusion.

Step II. Production of cracks on the surface of samples due to an increase in the water vapour pressure in the inner layers and emergence of channels for the vapour diffusion towards the surface. The density and size of cracks increase as the heating rate of the crystals increases. Dehydration of nickel sulfate hexa- and tetrahydrates to the dihydrate in the interior of the crystals.

Step III. Successive dehydration of the dihydrate to monohydrate and then to the anhydrous salt.

Based on the aforesaid, the factors that govern the laws of dehydration of α-$NiSO_4 \cdot 6H_2O$ are as follows:

— temperature interval of the dehydration;

— isothermal or non-isothermal character of the process;

— rate of changes in temperature for the non-isothermal process;

— vapour pressure over the sample surface and the composition of the atmosphere; the presence of water vapour is of importance;

— the mass and the specific surface area of the sample;

— structural perfection of the sample and first of all, the density of dislocations outcropping on the surface; and

— the state of the sample surface (depends on the specific features of mechanical treatment of the surface).

Based on analysis of published data, TGA experiments aimed at comparing the thermal stabilities of different crystals can give correct results if the following requirements are met:

— the heating rate, the composition of the atmosphere and the pressure should be the same for all samples under study; and

— to avoid the influence of structural features of the crystal surface, it is desired to determine the initial dehydration temperature using polycrystalline powders with specified grain size.

II.6. Growth of α-$NiSO_4 \cdot 6H_2O$ crystals

In one of the first studies on the growth of large α-$NiSO_4 \cdot 6H_2O$ crystals for optical filters[9] crystals were grown by cooling the solution from 53 to 33 °C using 1-mm-thick crystalline plate seeds glued onto crystal holders. Solutions were prepared using $NiSO_4 \cdot 6H_2O$ with a purity of 98.5% and stirred through reversible rotation of the growing crystal at a rate of 30 rpm. The cooling rate was 0.5 – 1 °C per day. The solution supersaturations and the growth rates of the habit-forming faces were not specified.[9] The spectroscopic properties of the crystals grown (crystal dimensions to $65 \times 85 \times 75$ mm) were studied using plates obtained by cleavage in the (001) cleavage plane. The transmission spectrum of α-$NiSO_4 \cdot 6H_2O$ sample 2 mm thick is shown in Fig. 6. Good UV transmittance is accompanied by high transmittance in the IR and visible regions, which can be due to the small thickens of the sample.

Later on, the method of directed growth of cylindrical α-$NiSO_4 \cdot 6H_2O$ crystals with diameters equal to that of the

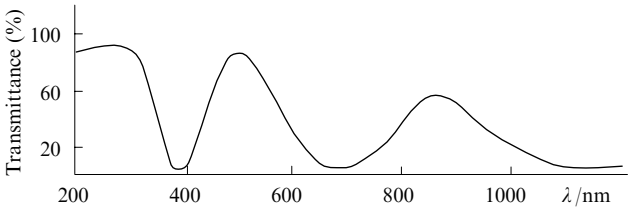


Figure 6. Transmission spectrum of crystalline α-$NiSO_4 \cdot 6H_2O$.[9]

desired optical elements was developed.[47] The solution was also prepared using $NiSO_4 \cdot 6H_2O$ with a purity of 98.5% and the temperature interval utilized was the same as that described in Ref. 9. A distinctive feature of the method consisted in that glass cylindrical crucibles of specified diameter with round seed plates glued onto the bottoms were placed on a number of platforms rotating about the same axis and fixed on a rotation bar. The entire system was placed into the crystallizer containing overheated solution and subsequent cooling of the solution, was accompanied by the growth of crystals along the [001] direction.

This crystallizer was suitable for growing of up to 12 cylindrical crystals 30–40 mm in diameter and 40 mm long in 1.5 months; the average normal growth rate of the (001) face was 1–1.5 mm day^{-1}. Optical elements fabricated from these crystals were characterized by rather high spectral characteristics, *e.g.*, the UV transmittance exceeded a value of 85%.[47] This study formed the basis of a patent [13] for the new method for growth of cylindrical α-$NiSO_4 \cdot 6H_2O$ crystals.

Based on analysis of the phase diagrams of the $NiSO_4-H_2SO_4-H_2O$ system, the compositions of the growth solutions prepared using nickel sulfate hexahydrate, nickel sulfate heptahydrate and anhydrous nickel sulfate were proposed.[48] The solution containing α-$NiSO_4 \cdot 6H_2O$ was acidified with sulfuric acid. Crystals were also grown by cooling the solution from 53 to 32 °C. No solution supersaturation and crystal face growth rates were reported. The structure of the α-$NiSO_4 \cdot 6H_2O$ crystal can be illustrated by an X-ray projection topograph of the (011) cut (Fig. ES.15). Distorted central region of the crystal, band-type structure of the growth sectors of the (012) and (113) faces, which characterizes a nonuniform impurity distribution between growth layers, and contrast sectorial boundaries are indicative of low structural perfection of the α-$NiSO_4 \cdot 6H_2O$ crystal.[48]

The influence of solution pH on the growth of α-$NiSO_4 \cdot 6H_2O$ crystals was studied in relation to solutions acidified with H_2SO_4 to pH 0.2 and acid-free solutions with pH 2.9.[49] All experiments were carried out under identical growth conditions (solution saturation temperatures and stirring regimes). The cooling rates of the solutions were chosen taking account of solubility data to allow crystals to grow under a constant supersaturation of $\sigma \approx 0.5\%$. The normal growth rates (R) of the [100], [010] and [001] crystal faces were $R_{[100]} = R_{[010]} = R_{[001]} \approx 1.1$ mm day^{-1} for the more acidic solutions and $R_{[100]} = R_{[010]} \approx 1.1$, $R_{[001]} \approx 1.5$ mm day^{-1} for the acid-free solutions. Both series of crystals had a habit shown in Fig. ES.5 and demonstrated no visible defects.

The development of a technology for rapid growth of α-$NiSO_4 \cdot 6H_2O$ crystals involved a research into the influence of different cooling regimes on the properties of crystals grown.[50, 51] Indeed, the following problems are unavoidably posed as the growth rate increases:

— impurities cause the formation of macrosteps and incorporation of solution inclusions; this adversely influences the optical properties of crystals;

— at high supersaturations, secondary seeding is highly probable; therefore, crystal growth is often accompanied by spontaneous crystallization leading to a decrease in the normal growth rates of crystal faces and the mass of the crystal.

To solve these problems is to grow crystals of good optical quality.

Two series of α-$NiSO_4 \cdot 6H_2O$ crystals were grown at high and low normal face growth rates from solutions with saturation temperatures of about ~50 °C under different cooling regimes. The solutions were prepared using domestic chemicals (chemically pure $NiSO_4 \cdot 7H_2O$ and sulfuric acid of high purity filtered through track-etched membranes with a pore diameter of 0.2 μm) and had the same composition. The growth experiments were conducted until cooling the solutions to room temperature using the same stirring regimes. The maximum cooling rate (v) was 5–7 °C day^{-1} for rapidly grown crystals and 0.5–1.5 °C day^{-1} for slowly grown ones. The normal growth rate of the [001] faces was $R_{[001]} \approx 5-7$ mm day^{-1} (rapid growth) and $R_{[001]} \approx 1.0-1.5$ mm day^{-1} (slow growth). The growth parameters of three crystals grown in one-litre crystallization vessels at different cooling rates are listed in Table 6.[50, 51]

The bulk of the α-$NiSO_4 \cdot 6H_2O$ crystal is mainly consists of two growth sectors, {011} (tetragonal bipyramid) and {001} (pinacoid). The optical transmission spectra of crystalline samples cut from these growth sectors of the rapidly grown and slowly grown crystals were recorded. The samples (plates 5 mm thick) were cleaved in the (001) cleavage plane. The best optical parameters were obtained for the {011} growth sector of the rapidly grown crystals; namely, its transmittance was 85%–86% at $\lambda = 200-370$ nm, being relatively low in the visible region (Fig. 7). The UV transmittance of the {001} sector of the rapidly grown crystals is comparable with that of the {011} and {001} sectors of the slowly grown crystals (75%–77%). The visible-region transmittance of both growth sectors of the slowly grown crystals is higher than that of the rapidly grown crystals.

Uncontrollable impurities present in crystals may influence their optical parameters. Therefore, impurities in the crystals in question were analyzed by spark mass spectrometry.[51] The concentrations of most impurities including Be,

Table 6. Growth parameters of α-$NiSO_4 \cdot 6H_2O$ crystals grown from aqueous solutions at different cooling rates.[50, 51]

v (see [a])	$R_{[001]}$ (see [b])	$R_{[100]} = R_{[010]}$ (see [b])	Growth time /day	m_{cryst} /g	Crystal dimensions $x \times y \times z$ /mm
0.6	1.3	1.1	27	185	65 × 51 × 35
5	5.5	6.5	4	125	52 × 52 × 22
5.5	7.0	7.7	4	190	63 × 60 × 28

[a] In °C day^{-1}; [b] in mm day^{-1}.

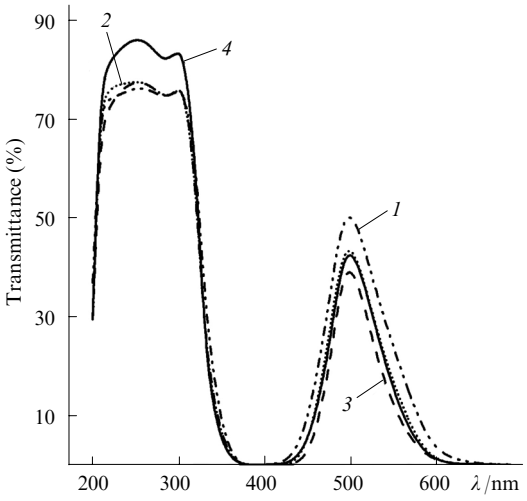


Figure 7. Transmission spectra of α-$NiSO_4 \cdot 6H_2O$ crystals grown at different rates.[51]
Growth sectors: {001} (*1*, *3*) and {011} (*2*, *4*) for the slowly (*1*, *2*) and rapidly (*3*, *4*) grown crystals.

Na, P, Sc, Ti, V, Cr, Mn, Ga, Ge, As, Se, Br, Rb, Sr, Y, Zr, Nb, Mo, Ru, Rh, Pd, Ag, Cd, In, Sn, Sb, Te, Cs, Ba, Hf, W, Re, Os, Ir, Pt, Au, Hg, Tl, Pb, Bi, Th, U and all lanthanides were lower than the limit of detection (less than 10^{-4} mass %). Data on the distribution of impurities whose concentrations exceed 10^{-4} mass % are listed in Table 7. According to the mass spectrometry data, the major impurities in the crystals in question include Zn, Co, Cu, I, F, Cl ($>10^{-3}$ mass %), while Mg, Ca, Fe, Al, Si, B are present in smaller amounts.

The impurity distributions in the α-$NiSO_4 \cdot 6H_2O$ crystals grown at different rates are different. From the data of Table 7 it follows that the maximum concentrations of Zn, Co, Cu, Al, Mg, B and I were found in the rapidly grown crystals. Therefore, based on the Burton–Prim–Slichter equation,[52] one can assume that the equilibrium distribution coefficients of these impurities do not exceed unity. The concentrations of Zn, Cu, Al and B {001} growth sector are several times higher than in the {011} sector. The reverse was observed for Mg and Co, *viz*., their concentrations in the {001} growth sector of the rapidly grown crystals were 1.5–2 times lower.[51] The slowly grown α-$NiSO_4 \cdot 6H_2O$ crystals were characterized by the same concentrations of impurities in both growth sectors. The concentrations of F and Cl in these crystals were higher than in the rapidly grown crystals.

Table 7. Impurity distribution in α-$NiSO_4 \cdot 6H_2O$ crystals grown by different methods.[51]

Impurity	Concentration (10^{-4} mass %)		
	rapidly grown crystal		slowly grown crystal
	{011} growth sector	{001} growth sector	{001} and {011} growth sectors
Li	<0.01	<0.01	0.08
B	0.4	1	0.05
F	20	20	30
Mg	10	6	3
Al	0.2	1	<0.07
Si	6	6	3
Cl	7	10	30
K	<0.1	<0.1	3
Ca	0.9	1	0.6
Fe	1	1	1
Co	50	20	10
Cu	10	20	<0.1
Zn	1000	2000	8
I	90	100	3

An analysis of the optical spectra and impurity concentrations in the samples revealed no correlations between the changes in transmittance and the concentration of a particular impurity.

One more possible reason for a decrease in transmittance is the presence of numerous scattering sites in the form of structural defects, *e.g*., inclusions, high inhomogeneity or sectorial boundaries. To compare the quality of the rapidly and slowly grown α-$NiSO_4 \cdot 6H_2O$ crystals, the real structure of the crystals was studied by Lang projection X-ray topography.[50, 51] Two topographs of the (100) cut of a slowly grown α-$NiSO_4 \cdot 6H_2O$ crystal are shown in Fig. 8. The {011} growth sector of this crystal contains clearly seen zonal inhomogeneity (ZI) stripes that may be a reason for the decrease in the transmission of this sector in the visible region compared with the transmission of the {001} sector. The {001} growth sector is characterized by numerous growth dislocations (D) directed from the seed (S) perpendicular to the (001) face. The presence of one vicinal-sectorial boundary (VSB) in this sector is indicative of only one growth hillock on the surface of the (001) face and, by and large, rather high homogeneity of this growth sector. Both topographs demonstrate the sectorial boundaries (SB) dividing different growth sectors.[51]

The real structure of the rapidly grown α-$NiSO_4 \cdot 6H_2O$ crystal is presented in Fig. 9 where the boundary between the {011} and {001} growth sectors has a brighter contrast. Taking into account the changes in the contrast at the sectorial boundary, one can conclude that the lattice constants or the {011} sector are smaller than for the {001} sector. No growth defects were observed in the {011}

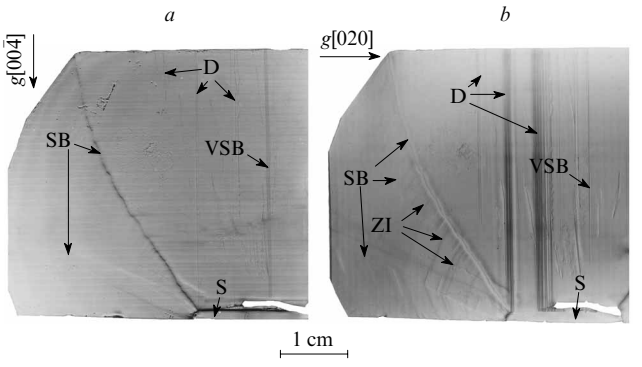


Figure 8. X-Ray projection topographs of the (100) cut of the slowly grown α-$NiSO_4 \cdot 6H_2O$ crystal at different diffraction vectors.[51]
For notations, see text.

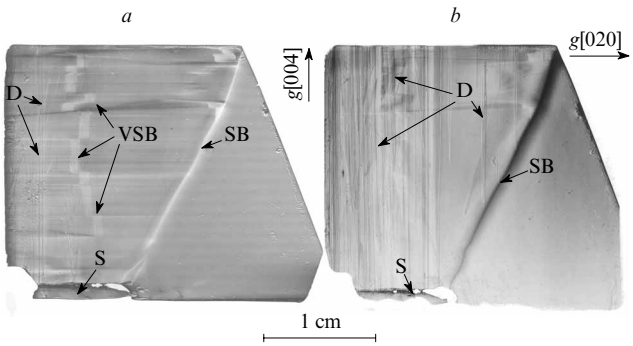


Figure 9. X-Ray projection topographs of the (100) cut of the rapidly grown α-$NiSO_4 \cdot 6H_2O$ crystal at different diffraction vectors.[51]

growth sector at both diffraction vectors. The concentration of growth dislocations in the {001} sector of the rapidly grown crystal is much higher than in the {001} sector of the slowly grown crystal. This is probably due to the fact that seed regeneration occurred at higher supersaturation. Usually, a high dislocation density leads to formation of multiple nucleation sites on crystal faces. The broken line in Fig. 9 *a* corresponds to VSB, thus indicating the presence of competing growth hillocks. Under these conditions, incorporation of solution inclusions is probable;[53] this causes more intense scattering of light, which seems to be the most likely reason for the decrease in the transmission of the sample cut from the {001} sector.[51]

The impurity distribution between two main growth sectors of the rapidly grown α-$NiSO_4 \cdot 6H_2O$ crystals is less uniform; however, analysis of the X-ray projection topographs showed that the {011} sector in these crystals is characterized by a higher degree of structural perfection compared to the corresponding sector of the slowly grown crystals. This is in good agreement with the maximum transmittance values obtained [51] for the {011} sector of the rapidly grown crystals. Therefore, it is the {011} sector of the rapidly grown crystals that seems to be the best candidate for application as UV filter. Improvement of the structural perfection and optical properties of the {001} sector requires optimization of the seed regeneration regime.

Using this method and 10-litre growth crystallizers, one can rapidly grow α-$NiSO_4 \cdot 6H_2O$ crystals of dimensions up to $140 \times 140 \times 90$ mm and a maximum mass of 2200 g within 30 days. The crystals grown contain no visible defects and provide a maximum UV transmittance (Fig. ES.16).[51]

Besides, a method and experimental design for the growth of α-$NiSO_4 \cdot 6H_2O$ single crystals under steady-state supercooling and forced convection of aqueous solution using shapers and without them have been proposed.‡ Here, the advantages consist in carrying out the process at a constant temperature under identical hydrodynamic conditions, which improves the quality of crystals grown. All the grown α-$NiSO_4 \cdot 6H_2O$ crystals exhibited no zonal inhomogeneity while the crystals grown in shapers also demonstrated no sectorial inhomogeneity because the growth occurred only along the (001) axis. The absence of zonal inhomogeneity can be explained by the fact that growth occurred under constant supersaturation, which excluded competition or the possibility of changing the growth sources.

‡ V M Masalov, A A Zhokhov, V L Manomenova, E B Rudneva, A E Voloshin, G A Emelchenko *Cryst. Rep.* **60** 963 (2015) [*Kristallografiya* **60** 981 (2015)].

III. Crystals of the nickel and cobalt families of double Tutton's salts

Double complex salts of the general formula $M^I_2M^{II}(SO_4)_2 \cdot 6H_2O$ (M^I = Cs, K, NH_4, Rb, Tl; M^{II} = Cd, Co, Cu, Fe, Mg, Mn, Ni, Zn; *i.e.*, transition metals) are known as Tutton's salts.§ Pioneering studies on the properties of solutions of these double salts and crystals $M^I_2M^{II}(SO_4)_2 \cdot 6H_2O$ date back to the late 19th century and the early 20th century;[54 – 59] however, these systems were out of use until the invention of solar-blind technology.

III.1. The phase diagrams of the $M^{II}SO_4 - M^I_2SO_4 - H_2O$ systems (M^{II} = Ni, Co; M^I = K, NH_4, Rb): an analysis

The $NiSO_4 - K_2SO_4 - H_2O$ system. The three-dimensional phase diagram of the ternary system $NiSO_4 - K_2SO_4 - H_2O$ was studied in the temperature range from 0 to 100 °C.[57] Its projection on the $s - T$ plane is presented in Fig. ES.17.

The system in question was also studied at 25 °C.[58]

The solubility diagram of the double salt $K_2Ni(SO_4)_2 \cdot 6H_2O$ at 55 °C is shown in Fig. 10.[59] The eutonic points *A* and *B* correspond to the solutions saturated with both salts, namely, K_2SO_4 and $K_2Ni(SO_4)_2 \cdot 6H_2O$ (point *A*), as well as α-$NiSO_4 \cdot 6H_2O$ and $K_2Ni(SO_4)_2 \cdot 6H_2O$ (point *B*). The line connecting the figurative points of water and $K_2Ni(SO_4)_2 \cdot 6H_2O$ (singular

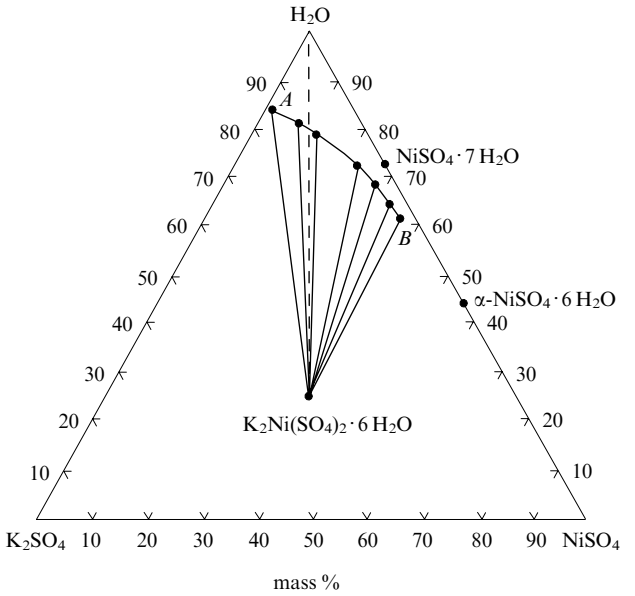


Figure 10. A part of the phase diagram of the $NiSO_4 - K_2SO_4 - H_2O$ system at 55 °C.[59]
Here and in Figs 11 – 13 *A*, *B* denote eutonic points and dashed line is the singular secant.

§ A E Tutton pioneered in studying nearly 80 compounds belonging to this class.

secant) crosses the solubility curve of $K_2Ni(SO_4)_2 \cdot 6H_2O$; this is a feature of the phase diagrams of the systems characterized by the formation of congruently soluble double salts.[60]

Fragments of the Schreinemakers diagrams of the $NiSO_4 - K_2SO_4 - H_2O$ system studied [58, 61] at 25 and 40 °C are presented in Fig. ES.18. The bent shape of the curves describing the solubility of K_2SO_4 in saturated $NiSO_4$ solutions and the solubility of $NiSO_4$ in saturated K_2SO_4 solutions indicates that the addition of a salt causes the solubility of the other salt to increase. A characteristic feature of these Schreinemakers diagrams is the short solubility curve of $NiSO_4$ in saturated K_2SO_4 solution.

The $NiSO_4 - (NH_4)_2SO_4 - H_2O$ system. The three-dimensional phase diagram of the ternary system $NiSO_4 - (NH_4)_2SO_4 - H_2O$ was studied in the temperature interval from 0 to 100 °C.[57] Its projection on the $s - T$ plane is shown in Fig. ES.19.

Figure ES.20 presents the solubility isotherm of the system in question at 25 °C.[62]

The solubility diagram of the double salt $(NH_4)_2Ni(SO_4)_2 \cdot 6H_2O$ at 46 °C is shown in Fig. 11.

An analysis of the solubility diagrams of the $NiSO_4 - (NH_4)_2SO_4 - H_2O$ system showed that double salt $(NH_4)_2Ni(SO_4)_2 \cdot 6H_2O$ crystallizes in the temperature interval 0 – 100°C in a wide range of component concentrations.

The $NiSO_4 - Rb_2SO_4 - H_2O$ system. The results of investigations of the phase diagram of the $NiSO_4 - Rb_2SO_4 - H_2O$ system in the temperature interval 0 – 100 °C are presented in Fig. ES.21.[57]

The solubility isotherms of the double salt $Rb_2Ni(SO_4)_2 \cdot 6H_2O$ at 0, 25 and 100 °C (see Fig. 12) were reported in Ref. 63 with reference to Ref. 64. The solubility of this double salt considerably increases with increasing temperature.

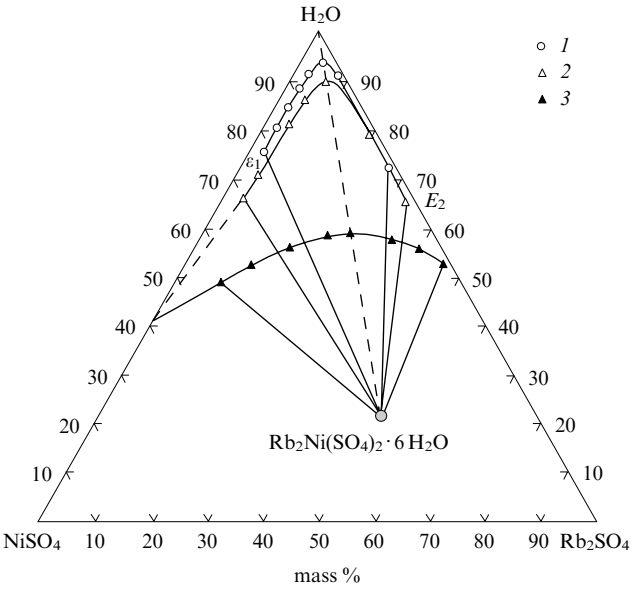


Figure 12. A part of the phase diagram of the $Rb_2SO_4 - NiSO_4 - H_2O$ system at 0 (*1*), 25 (*2*) and 100 °C (*3*).[63]

The $NiSO_4 - Cs_2SO_4 - H_2O$ system. No data on the $NiSO_4 - Cs_2SO_4 - H_2O$ system were found in the literature. It seems not unreasonable to assume that, since compound $Cs_2Ni(SO_4)_2 \cdot 6H_2O$ belongs to the isotypic series of compounds $M^I_2Ni(SO_4)_2 \cdot 6H_2O$, it also represents a congruently soluble salt and crystallizes in a wide interval of temperatures and component concentrations.

The $CoSO_4 - K_2SO_4 - H_2O$ system. The three-dimensional phase diagram of the ternary system $CoSO_4 - K_2SO_4 - H_2O$ (see Fig. ES.22) was studied in the

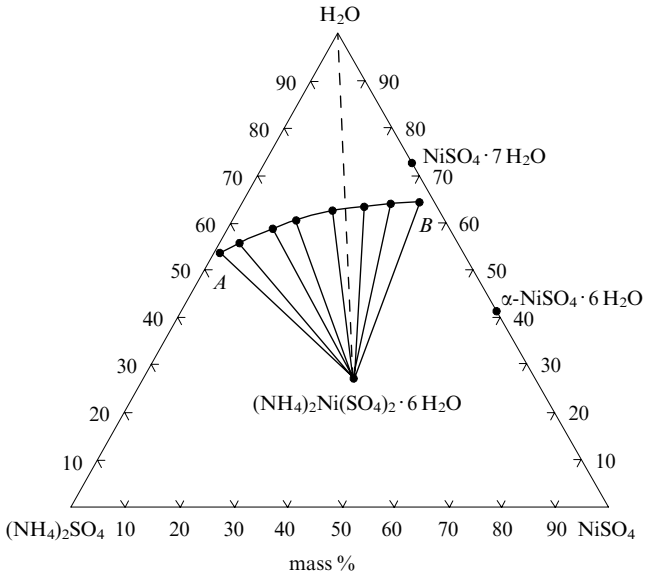


Figure 11. A part of the phase diagram of the $NiSO_4 - (NH_4)_2SO_4 - H_2O$ system at 46 °C.[59]

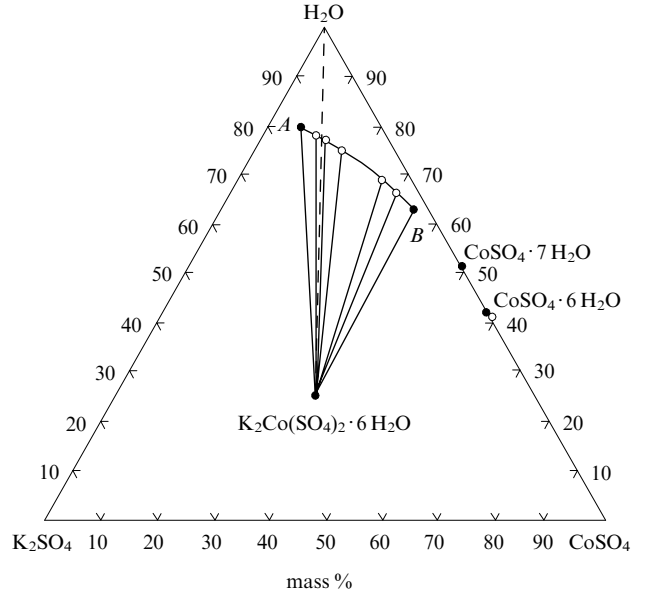


Figure 13. A part of the phase diagram of the $CoSO_4 - K_2SO_4 - H_2O$ system at 50 °C.[59]

temperature range from 0 to 100 °C.[65,66] Its projection on the $s-T$ plane is demonstrated in Fig. ES.23.[57] The only difference between the published results[57,65] is as follows: the $K_2Co(SO_4)_2\cdot 4H_2O$ phase was not observed in Ref. 57, whereas the authors of Ref. 65 did observe it in the 99.5–100 °C temperature interval.

Figure 13 presents a portion of the solubility diagram of the $CoSO_4-K_2SO_4-H_2O$ system at 50 °C corresponding to the solubility branch of the hexahydrate $K_2Co(SO_4)_2\cdot 6H_2O$.[59] The eutonic points *A* and *B* correspond to the solutions saturated with both salts, namely, K_2SO_4 and $K_2Co(SO_4)_2\cdot 6H_2O$ (point *A*), $CoSO_4\cdot 7H_2O$ and $K_2Co(SO_4)_2\cdot 6H_2O$ (point *B*).

The line connecting the figurative points of water and $K_2Co(SO_4)_2\cdot 6H_2O$ (singular secant) crosses the solubility branch of $K_2Co(SO_4)_2\cdot 6H_2O$, thus indicating congruent solubility of the double salt.[60]

Recently, there has been a renewed interest of researchers in the ternary system in question. Like the addition of K_2SO_4 to saturated solutions of $CoSO_4$, the introduction of $CoSO_4$ into saturated aqueous K_2SO_4 solutions (Fig. ES.24)[61] causes the solubilities of both salts to increase (this is analogous to the situation for the $K_2SO_4-NiSO_4-H_2O$ system, see above). An analysis of the diagrams of phase equilibria in the $K_2SO_4-CoSO_4-H_2O$ system revealed stable crystallization of the congruently soluble solid phase $K_2Co(SO_4)_2\cdot 6H_2O$ in a wide range of component concentrations in the temperature interval from 0 to 96 °C.

III.2. The solubility of double Tutton's salts in water

Table 8 presents the solubilities of double Tutton's salts $M^I_2M^{II}(SO_4)_2\cdot 6H_2O$ (M^I = K, NH_4, Rb; M^{II} = Ni, Co) in water.

An analysis of the phase diagrams of the ternary systems (see above) suggests that:

— double salts $K_2Co(SO_4)_2\cdot 6H_2O$, $K_2Ni(SO_4)_2\cdot 6H_2O$, $(NH_4)_2Ni(SO_4)_2\cdot 6H_2O$ and $Rb_2Ni(SO_4)_2\cdot 6H_2O$ belong to congruently soluble compounds;

— Tutton's salts $M^I_2M^{II}(SO_4)_2\cdot 6H_2O$ (M^I = K, NH_4, Rb; M^{II} = Ni, Co) are formed in a wide range of component concentrations; crystallization is possible in the temperature interval from 0 to 100 °C for the nickel salts and from 0 to 98 °C for $K_2Co(SO_4)_2\cdot 6H_2O$;

— among the double salts considered, $K_2Co(SO_4)_2\cdot 6H_2O$ exhibits the maximum solubility in water; for the nickel salts, the solubility of $(NH_4)_2Ni(SO_4)_2\cdot 6H_2O$ is somewhat higher than that of $K_2Ni(SO_4)_2\cdot 6H_2O$ and $Rb_2Ni(SO_4)_2\cdot 6H_2O$.

The phase diagrams of the $NiSO_4-H_2SO_4-H_2O$ and $M^{II}SO_4-M^I_2SO_4-H_2O$ (M^I = K, NH_4, Rb; M^{II} = Ni, Co) systems were also analyzed in a monograph.[68]

III.3. The habit and structure of $M^I_2M^{II}(SO_4)_2\cdot 6H_2O$ crystals

The crystal habit of double Tutton's salts is shown in Fig. ES.25.[32]

The crystal structures of $K_2Ni(SO_4)_2\cdot 6H_2O$, $(NH_4)_2Ni(SO_4)_2\cdot 6H_2O$, $Rb_2Ni(SO_4)_2\cdot 6H_2O$, $Cs_2Ni(SO_4)_2\cdot 6H_2O$ and $K_2Co(SO_4)_2\cdot 6H_2O$ were studied.[69–80] These compounds form an isotypic series and crystallize in the monoclinic system (space group $P2_1/c$, $Z=2$. The structure of $M^I_2M^{II}(SO_4)_2\cdot 6H_2O$ crystals represents a framework of complex octahedral cations $[M^{II}(H_2O)_6]^{2+}$ linked to SO_4^{2-} tetrahedra through hydrogen bonds; each water molecule forms hydrogen bonds with two oxygen atoms belonging to two different sulfate groups. Alkali metal cations are located within the framework. In the M^IO_8 polyhedron, each M^I cation is surrounded by six oxygen atoms of sulfate groups and two oxygen atoms of water molecules (Fig. ES.26).

A structural feature of crystals containing ammonium cation instead of alkali metal cation consists in the presence of additional hydrogen bonds between NH_4^+ and SO_4^{2-} groups.[70,75–77] The unit cell parameters of selected crystals of double Tutton's salts are listed in Table 9.

Structural transformations occurring in the series of compounds $K_2M^{II}(SO_4)_2\cdot 6H_2O$, $Rb_2M^{II}(SO_4)_2\cdot 6H_2O$ and $Cs_2M^{II}(SO_4)_2\cdot 6H_2O$ (M^{II} = Mg, Mn, Fe, Co, Ni and Zn) with increasing radius of transition metal cation were analyzed.[71,74,78] However, the influence of the radius of the alkali metal cation on the crystal structure of salts $M^I_2Ni(SO_4)_2\cdot 6H_2O$ and $M^I_2Co(SO_4)_2\cdot 6H_2O$ has not been studied until recently.

To make such an analysis for compounds $M^I_2Ni(SO_4)_2\cdot 6H_2O$ possible, the crystal structures of $Cs_2Ni(SO_4)_2\cdot 6H_2O$ and $Rb_2Ni(SO_4)_2\cdot 6H_2O$ were refined.[79,80] The X-ray diffraction experiment details are summarized in Table 10. In the first step, hydrogen atoms were omitted and the atomic coordinates (for all atoms except nickel atoms occupying specific positions), the scale factor, the isotropic extinction parameter and the thermal vibration parameters were refined anisotropically.

Hydrogen atoms were located from the difference electron density syntheses using the calculated and experimental structural amplitudes. The maximum residual peaks lying no further than 1 Å from oxygen atoms of water molecules were taken as coordinates of hydrogen atoms. Finally, all structural parameters determined earlier, the coordinates of hydrogen atoms and the isotropic thermal parameters were refined altogether.

Selected crystallographic parameters of the $Rb_2Ni(SO_4)_2\cdot 6H_2O$ and $Cs_2Ni(SO_4)_2\cdot 6H_2O$ crystals[79,80] as well as the results of previous studies are listed in Table 11.

Table 8. Solubilities of double Tutton's salts.[57,67]

Salt	Solubility (g per 100 g H_2O) at temperature /°C										
	0	10	20	30	40	50	60	70	80	90	100
$K_2Co(SO_4)_2\cdot 6H_2O$	8.5	11.7	15.5	19.4	23.4	27.7	32.5	38.7	47.8	–	–
$K_2Ni(SO_4)_2\cdot 6H_2O$	3.5	4.5	6.0	7.7	9.9	12.4	15.4	18.8	22.9	27.8	33.5
$(NH_4)_2Ni(SO_4)_2\cdot 6H_2O$	4.2	5.4	6.9	7.8	11.2	15.3	17.3	21.2	25.9	31.4	38.0
$Rb_2Ni(SO_4)_2\cdot 6H_2O$	2.7	3.8	5.2	7.0	9.2	11.9	15.0	18.8	23.5	28.4	34.5

Table 9. Unit cell parameters of double Tutton's salts.

Crystal	Effective radius of M^I cation /Å (see [a])	Unit cell parameters					Ref.
		a /Å	b /Å	c /Å	β /deg	V /Å^3	
$K_2Ni(SO_4)_2 \cdot 6H_2O$	1.38	6.1368(5)	12.1904(8)	9.0049(4)	105.047(5)	650.56(8)	74
$(NH_4)_2Ni(SO_4)_2 \cdot 6H_2O$	1.48	6.244(2)	12.469(4)	9.195(3)	106.98(3)	684.68	70
$Rb_2Ni(SO_4)_2 \cdot 6H_2O$	1.52	6.221(2)	12.410(2)	9.131(2)	106.06(2)	677.5	71
$Cs_2Ni(SO_4)_2 \cdot 6H_2O$	1.67	6.358(1)	12.767(2)	9.259(2)	107.00(2)	718.7	78
$K_2Co(SO_4)_2 \cdot 6H_2O$	1.38	6.155(1)	12.211(2)	9.057(1)	104.82(1)	658.0(3)	72

[a] Data taken from Refs 81 and 82.

Table 10. X-Ray experiment details for structure refinement of $Rb_2Ni(SO_4)_2 \cdot 6H_2O$ and $Cs_2Ni(SO_4)_2 \cdot 6H_2O$ single crystals.[79, 80]

Condition	$Rb_2Ni(SO_4)_2 \cdot 6H_2O$	$Cs_2Ni(SO_4)_2 \cdot 6H_2O$
Sample diameter /mm	0.25(1)	0.24(1)
Diffractometer	X Calibur S	ENRAF-NONIUS CAD-4F
Radiation	Mo K_α	Mo K_α
θ_{max} /deg	66.52	44.71
Number of parameters to be refined	162	182
$R1$ (%) (see [a])	1.78	1.71
$R2$ (%) (see [b])	2.81	1.95
Software	JANA 2000	JANA 98

[a] Normal convergence factor.
[b] Weight-average convergence factor.

A comparison of the results of X-ray diffraction studies [79, 80] with the results obtained earlier [71, 78] showed that the relative differences between the unit cell parameters are at most 7×10^{-2} %. A fragment of the crystal structures of $Rb_2Ni(SO_4)_2 \cdot 6H_2O$ and $Cs_2Ni(SO_4)_2 \cdot 6H_2O$ (hydrogen atoms are omitted) is shown in Fig. 14.

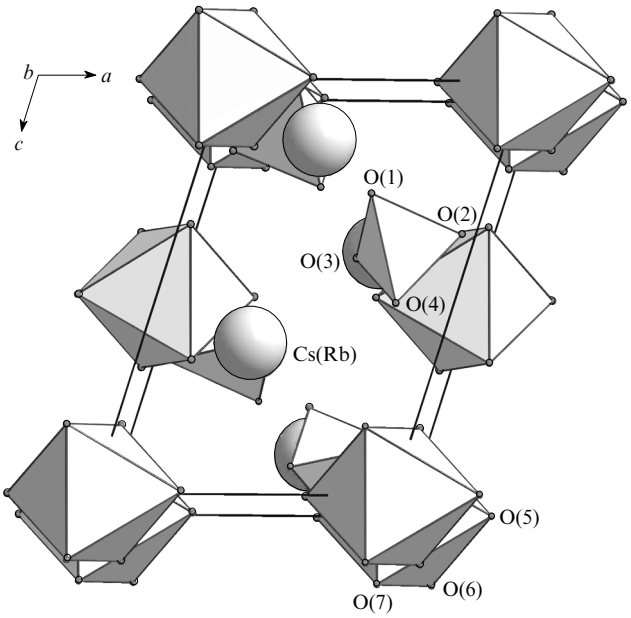


Figure 14. A fragment of the crystal structure of $Rb_2Ni(SO_4)_2 \cdot 6H_2O$ and $Cs_2Ni(SO_4)_2 \cdot 6H_2O$.[80]

III.4. Optical properties of $M^I_2M^{II}(SO_4)_2 \cdot 6H_2O$ crystals

Crystals of Tutton′s salts are optically biaxial. Positions of the axes of optical indicatrices and the refractive indices at a wavelength of 589 nm for the crystals $K_2Co(SO_4)_2 \cdot 6H_2O$, $K_2Ni(SO_4)_2 \cdot 6H_2O$, $(NH_4)_2Ni(SO_4)_2 \cdot 6H_2O$, $Rb_2Ni(SO_4)_2 \cdot 6H_2O$ and $Cs_2Ni(SO_4)_2 \cdot 6H_2O$ are listed in Table 12.[32]

Table 11. Selected crystallographic parameters of $Rb_2Ni(SO_4)_2 \cdot 6H_2O$ and $Cs_2Ni(SO_4)_2 \cdot 6H_2O$ crystals.

Parameter	$Rb_2Ni(SO_4)_2 \cdot 6H_2O$ (see [a])		$Cs_2Ni(SO_4)_2 \cdot 6H_2O$ (see [b])	
a /Å	6.2219(9)	6.221(2)	6.3576(8)	6.358(1)
b /Å	12.4053(17)	12.410(2)	12.7660(17)	12.767(2)
c /Å	9.1368(12)	9.131(2)	9.2550(10)	9.259(2)
β /deg	106.082(12)	106.06(2)	106.97(1)	107.00(2)
V /Å^3	677.6	677.5	718.4	718.7
ρ /g cm^{-3}	2.60	2.60	2.88	2.88

Note. For both crystals, all studies cited here report the following: monoclinic crystal system, space group $P2_1/c$, $z = 2$.
[a] Left column: data taken from Ref. 80; right column: data taken from Ref. 71.
[b] Left column: data taken from Ref. 79; right column: data taken from Ref. 78.

Like the optical absorption spectrum of α-$NiSO_4 \cdot 6H_2O$ crystal, those of crystals of the nickel family of Tutton′s salts should obey the pattern specified by the Ni d^8-ion in the octahedral field of water molecules (*i.e.*, by the $[Ni(H_2O)_6]^{2+}$ cation). This hypothesis was confirmed experimentally, namely, a study [18] on the absorption spectra of $(NH_4)_2Ni(SO_4)_2 \cdot 6H_2O$, $K_2Ni(SO_4)_2 \cdot 6H_2O$ and $Rb_2Ni(SO_4)_2 \cdot 6H_2O$ crystals in the 250 – 1000 nm wavelength range revealed their similarity between them and the transmission spectrum of α-$NiSO_4 \cdot 6H_2O$ crystal. Indeed, these crystals exhibit three absorption bands whose maxima are close to the absorption maxima of α-$NiSO_4 \cdot 6H_2O$ in this wavelength range (Table 13).

Note that the absorption spectrum of an ion is not identical to that of a crystal. The reasons are as follows: the crystal structure is comprised of different ions, and the absorption spectrum of each ion contributes to the absorption spectrum of the crystal; the formation of a crystal causes the energy levels of individual ions to split in the crystal field, which leads to broadening of absorption lines

Table 12. Optical parameters of crystals of Tutton's salts.[32]

Crystal	Positions of the axes of optical indicatrices				Refractive indices at λ = 589 nm			
	$\widehat{cN_p}$	$N_p\widehat{\{20\bar{1}\}}$	N_m	$2W$	n_p	n_m	n_g	$n_g - n_p$
$K_2Co(SO_4)_2 \cdot 6H_2O$	10°5′	31°12′	*b*	68°41′	1.4807	1.4865	1.5004	0.0197
$K_2Ni(SO_4)_2 \cdot 6H_2O$	8°42′	32°34′	*b*	75°16′	1.4836	1.4916	1.5051	0.0215
$(NH_4)_2Ni(SO_4)_2 \cdot 6H_2O$	5°12′	36°40′	*b*	86°33′	1.4949	1.5007	1.5081	0.0132
$Rb_2Ni(SO_4)_2 \cdot 6H_2O$	12°38′	28°49′	*b*	82°0′	1.4895	1.4961	1.5052	0.0157
$Cs_2Ni(SO_4)_2 \cdot 6H_2O$	24°7′	17°27′	*b*	−87°21′	1.5087	1.5129	1.5162	0.0075

Note. N_p, N_m are the axes of optical indicatrices; $2W$ is the angle between the optical axes in the crystals; n_p, n_m, n_g are the refractive indices.

Table 13. Positions of absorption maxima of $M^I_2Ni(SO_4)_2 \cdot 6H_2O$ crystals in the 250 – 1000 nm wavelength region.

Crystal	Positions of absorption maxima (in nm) corresponding to transitions			Ref.
	$^3A_{2g} \rightarrow {}^3T_{1g}(P)$	$^3A_{2g} \rightarrow {}^3T_{1g}(F)$	$^3A_{2g} \rightarrow {}^1E_g(D)$	
$(NH_4)_2Ni(SO_4)_2 \cdot 6H_2O$	385	644	706	18
$K_2Ni(SO_4)_2 \cdot 6H_2O$	385	643	707	18
$Rb_2Ni(SO_4)_2 \cdot 6H_2O$	385	642	708	18
α-$NiSO_4 \cdot 6H_2O$	386	649	708	34

(or narrow bands) of ions; additional broadening originates from thermal motion of atoms. Therefore, in contrast to linear absorption spectra of individual ions, those of crystals are band-like.

The absorption spectra of $M^I_2Ni(SO_4)_2 \cdot 6H_2O$ (M^I = K, NH_4, Rb) crystals in the 250 – 1000 nm wavelength range are schematically shown in Fig. ES.27.[18]

Earlier,[17] the spectroscopic parameters of $(NH_4)_2Ni(SO_4)_2 \cdot 6H_2O$ crystal were investigated with emphasis placed on the IR region; the absorption maxima were located at 392, 633, 709 and 1124 nm. This is somewhat different from the results obtained in another study.[18]

Long after then,[10, 83] the wavelength range of spectroscopic studies of $K_2Ni(SO_4)_2 \cdot 6H_2O$ crystal was also extended to 200 – 1400 nm; however, positions of absorption maxima in the IR region were not reported because the primary attention was paid to transmission bands.

The absorption spectrum of $K_2Co(SO_4)_2 \cdot 6H_2O$ crystal is specified by the Co^{2+} d^7-ion in the octahedral field of water molecules. Based on the energy level diagram of the Co^{2+} ion in octahedral field (Fig. 15 *a*),[37] there should be three spin-allowed d – d-transitions of this ion from the $^4T_1(F)$ ground state to the $^4T_{2g}$, $^4A_{2g}$ and $^4T_{1g}(P)$ states.

The absorption spectrum of $[Co(H_2O)_6]^{2+}$ ion in the visible region is shown in Fig. 15 *b*. The absorption band observed corresponds to the $^4T_1(F) \rightarrow {}^4T_{1g}(P)$ transition at ~540 nm; the $^4T_1(F) \rightarrow {}^4T_{2g}$ transition at 8350 cm^{-1} (1200 nm) is not shown. The $^4T_1(F) \rightarrow {}^4A_{2g}$ transition at ~560 nm is weak, close to the $^4T_1(F) \rightarrow {}^4T_{1g}(P)$ band and therefore not observed.[37]

The results of a study [84] on spectroscopic parameters of $K_2Co(SO_4)_2 \cdot 6H_2O$ crystals (Fig. ES.28) are in good agreement with those of theoretical calculations.[37]

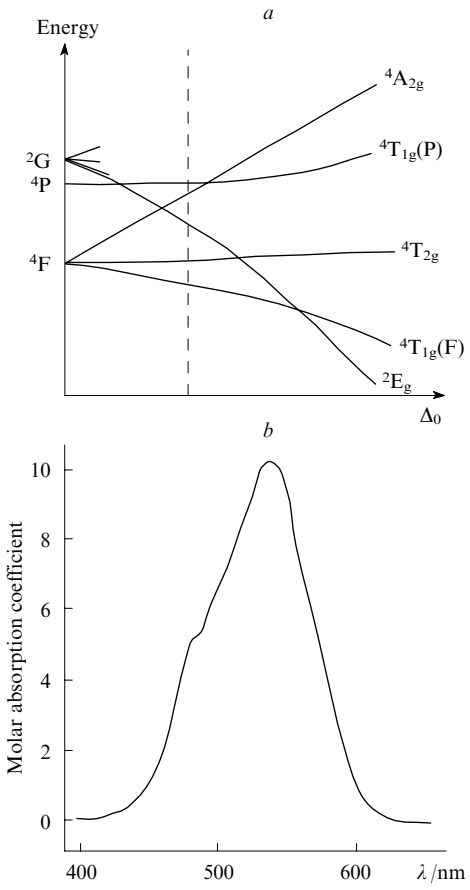


Figure 15. A fragment of the energy level diagram for a d^7 ion (Co^{2+}) in octahedral field (*a*) and the absorption spectrum of $[Co(H_2O)_6]^{2+}$ in the visible region (*b*);[37] Δ_0 is splitting of one-electron orbitals.

III.5. Growth of $M^I_2M^{II}(SO_4)_2 \cdot 6H_2O$ crystals

The $K_2Ni(SO_4)_2 \cdot 6H_2O$ and $(NH_4)_2Ni(SO_4)_2 \cdot 6H_2O$ crystals. The growth of $K_2Ni(SO_4)_2 \cdot 6H_2O$ and $(NH_4)_2Ni(SO_4)_2 \cdot 6H_2O$ crystals was studied.[10, 11, 59, 85] A

number of methods for growth of these crystals were patented.[12, 14, 15]

Researchers from the Russian Federation reported a pioneering study[59] on the growth of $K_2Ni(SO_4)_2\cdot 6H_2O$, $(NH_4)_2Ni(SO_4)_2\cdot 6H_2O$ and $K_2Co(SO_4)_2\cdot 6H_2O$ crystals. These results were not patented. Crystals were grown by cooling solutions at low supersaturations; the cooling rate was at most 0.02 °C day^{-1}. Based on an original procedure developed earlier,[86] it was proposed to grow crystals of Tutton's salts from solutions whose compositions lie on the solubility curve of $M^{I}_2M^{II}(SO_4)_2\cdot 6H_2O$ and are equidistant from two eutonic points. As a consequence, the component concentrations in the solutions were significantly different from stoichiometric values. For instance, the concentration of nickel sulfate in the growth solution for $K_2Ni(SO_4)_2\cdot 6H_2O$ was on the average twice as high as the stoichiometric value, the concentration of $(NH_4)_2SO_4$ in the growth solution for $(NH_4)_2Ni(SO_4)_2\cdot 6H_2O$ was 1.7 times higher and the content of cobalt sulfate in the growth solution for $K_2Co(SO_4)_2\cdot 6H_2O$ was also twice as high as the stoichiometric concentration. This procedure for the choice of solution compositions has the right to exist taking into account wide crystallization ranges of the double salts $M^{I}_2M^{II}(SO_4)_2\cdot 6H_2O$; however, it is hard to assess its benefits and drawbacks because the optical properties and structural perfection of the crystals grown[59] were not studied.

'Northrop Grumman Corporation' (USA) patented a method of growth and an application of $K_2Ni(SO_4)_2\cdot 6H_2O$ crystals as UV filters.[14] The salt, $K_2Ni(SO_4)_2\cdot 6H_2O$, was dissolved in a mixture of hydrochloric acid and water (30 : 70). It was stated that the solubility of the salt at such a high concentration of the acid was reasonably high. Crystal growth of $K_2Ni(SO_4)_2\cdot 6H_2O$ was carried out by cooling the solution in the temperature interval from 40 to 25 °C. The average cooling rate was rather high ($\sim$1.2 °C day^{-1}) and maintained constant throughout the growth process. It was reported that low pH value of the solution (pH $<$6.0, see text of the patent) helped to avoid spontaneous nucleation at the bottom of the crystallizer. The composition of crystals grown was confirmed by X-ray powder diffraction. A study of spectroscopic properties revealed an UV transmittance of the order of 5%, which indicated a low optical quality of the crystals patented.

In another study[10] $K_2Ni(SO_4)_2\cdot 6H_2O$ crystals were grown from stoichiometric solutions acidified with hydrochloric acid to reach pH 2.0 using stick-shaped crystals extended along the x axis as seeds. Crystals were grown at high supersaturations ($\sigma = 4\%-7\%$), that caused disappearance of {011} and {100} faces, although they were well-defined under low supersaturations. At low growth rates, it is these sectors that contained a maximum amount of solution inclusions; the authors believed this led to considerably reduce the concentration of these structural defects. The maximum UV transmittance of the $K_2Ni(SO_4)_2\cdot 6H_2O$ crystals grown was 85%; clearly, such a high value was due to the small thickness of the samples (2 mm).[10]

A patent for the method for growth of $(NH_4)_2Ni(SO_4)_2\cdot 6H_2O$ crystals and their application as optical band-pass UV filters belongs to 'Inrad' (USA).[15] From the description of the invention it follows that growth solutions were prepared using a mixture of equimolar amounts of components, $NiSO_4$ and K_2SO_4, and pure distilled water as solvent. Crystal growth was carried out by cooling the solution; the cooling rate was 0.05 °C day^{-1} to reach 2 °C in the final step of the growth process. The composition of the crystals grown was confirmed by chemical analysis and powder X-ray diffraction. The $(NH_4)_2Ni(SO_4)_2\cdot 6H_2O$ crystals grown by the method patented were of good optical quality, namely, the UV transmittance of a crystalline sample 4 mm thick was as high as 85%.[15]

Yet another study[11] on the growth of $(NH_4)_2Ni(SO_4)_2\cdot 6H_2O$ crystals, which was published simultaneously with the patent,[15] served as basis to a patent[12] belonging to researchers from People's Republic of China. Crystals were grown from stoichiometric solutions (pH 4.5) using a point seed immobilized on a rod rotating at 50 rpm. Solutions were cooled at rates of 0.2–0.5 °C per day. The average growth rates of crystal faces along the crystallographic axes x, y and z were 1.5, 2.2 and 2.2 mm day^{-1}, respectively. The UV transmission of 7-mm-thick samples cut from the crystals was 75%.[12]

To carry out controlled growth of $(NH_4)_2Ni(SO_4)_2\cdot 6H_2O$ crystals, researchers from this group also proposed[85] to improve the design of the crystallizer with a magnetic weight sensor for *in situ* calculations of the solution density and thus the actual solution concentration at any time.

Later,[87] the influence of the composition of growth solution on the growth rates of $(NH_4)_2Ni(SO_4)_2\cdot 6H_2O$ and $K_2Ni(SO_4)_2\cdot 6H_2O$ crystal faces was studied. The average initial solution supersaturations (no acids added) were $\sim$0.5%–0.8%. Attempts to achieve higher supersaturations led to spontaneous secondary nucleation and growth of 'parasitic' crystals on the platform and on the bottom of the crystallizer. The growth rates of the crystal faces abruptly decreased due to the decrease in the supersaturation. Earlier,[10] it was emphasized that $K_2Ni(SO_4)_2\cdot 6H_2O$ crystals were grown from solutions acidified with hydrochloric acid to pH 2. Similar experiments on solution growth of $(NH_4)_2Ni(SO_4)_2\cdot 6H_2O$ and $K_2Ni(SO_4)_2\cdot 6H_2O$ crystals (acidification with HCl; controlled supersaturations in the range from 0.5% to 1.5%) gave samples characterized by low transparency and an UV transmittance of at most 20%.[87]

Acidification of growth solutions with H_2SO_4 (pH 2–2.5) allowed one to reach an initial supersaturation of 1.0%–1.2% (no spontaneous nucleation) with no decrease in the UV transmittance. At solution velocities of $\sim$15–20 cm s^{-1}, the average normal growth rates of the (100), (010) and (001) faces of $(NH_4)_2Ni(SO_4)_2\cdot 6H_2O$ crystal ($R_{(100)}$, $R_{(010)}$, $R_{(001)}$) were at most 1.1, 1.4, 0.8 mm day^{-1}, respectively, at a solution supersaturation of $\sim$0.8%–1.0%. The average normal growth rates of $K_2Ni(SO_4)_2\cdot 6H_2O$ crystal faces determined at nearly the same supersaturation and solution velocity were lower, namely, $R_{(100)} \leqslant 0.8$, $R_{(010)} \leqslant 1.0$ and $R_{(001)} \leqslant 0.5$ mm day^{-1}. In some cases, the {010}, {100} and {201} growth sectors of both $(NH_4)_2Ni(SO_4)_2\cdot 6H_2O$ and $K_2Ni(SO_4)_2\cdot 6H_2O$ samples contained small inclusions of mother solution.[87]

After a series of experiments, single crystals $(NH_4)_2Ni(SO_4)_2\cdot 6H_2O$ and $K_2Ni(SO_4)_2\cdot 6H_2O$ of good optical quality were grown. The average dimensions along the principal crystallographic axes were $60\times 70\times 45$ mm.

The maximum mass of crystals grown in a 5-litre crystallizer was 360 g (Figs ES.29 and ES.30).

The $Rb_2Ni(SO_4)_2\cdot 6H_2O$ and $Cs_2Ni(SO_4)_2\cdot 6H_2O$ crystals. A research group from the Russian Federation reported a number of studies on the growth of large single crystals of $Rb_2Ni(SO_4)_2\cdot 6H_2O$ from solutions with pH 2–2.5.[80,87,88] The maximum solution supersaturations not accompanied by spontaneous nucleation were ~1.0%–1.2% at solution velocities of ~15–20 cm s^{-1}. Under these conditions, the average normal growth rates, R_x, R_y and R_z, of crystal faces were 0.3, 0.4 and 0.17 mm day^{-1}, respectively. Attempts to increase the supersaturation led to formation of mother solution inclusions in the {010}, {100} and {201} growth sectors.

Eventually, experiments with 1.8-litre crystallizers gave transparent single crystals of $Rb_2Ni(SO_4)_2\cdot 6H_2O$ with dimensions to $25\times 30\times 20$ mm along the principal crystallographic axes (Fig. ES.31). The UV transmittance of 10 mm thick samples was as high as 80%.

The authors of three more recent studies[63,89,90] proposed their original methods for the growth of $(NH_4)_2Ni(SO_4)_2\cdot 6H_2O$ and $K_2Ni(SO_4)_2\cdot 6H_2O$ crystals[10,11,59] (see above) to grow mixed crystals of $Rb_2Ni(SO_4)_2\cdot 6H_2O$.

In Refs 63 and 89, recommendations to grow $Rb_2Ni(SO_4)_2\cdot 6H_2O$ crystals from a solution whose composition corresponds to points lying at equal distances from the eutonic lines were rejected. The proposed compositions of the growth solutions lie on the singular secant connecting $M_2Ni(SO_4)_2\cdot 6H_2O$ to H_2O, thus being stoichiometric compositions. Crystals were grown by cooling the solution; however, the solution supersaturations and the growth rates of crystal faces were not reported.

Growth of $Rb_2Ni(SO_4)_2\cdot 6H_2O$ crystals was carried out[90] in a solution acidified to pH 2.5; the method was just like that describe earlier.[11] The average growth rates of crystal faces were 1.8, 1.5 and 0.9 mm day^{-1} along the x, y and z axes, respectively. The UV transmittance of a 1.1-mm-thick sample cut from the $Rb_2Ni(SO_4)_2\cdot 6H_2O$ crystal was as high as 85%.

A method for growth of large single crystals of $Cs_2Ni(SO_4)_2\cdot 6H_2O$ of good optical quality was developed.[79,87,88,91–94] In the first series of growth experiments, pH values of mother liquors were in the range 3.5–4.0. At solution velocities of ~15–20 cm s^{-1}, the average normal growth rates, R_x, R_y and R_z, of crystal faces were at most 1.5, 1.7 and 0.5 mm day^{-1}, respectively, at solution supersaturations of 1.0%–1.2%.[87,88] The $Cs_2Ni(SO_4)_2\cdot 6H_2O$ crystals grown in this series of experiments contained inclusions of mother solution, mainly in the {201}, {010} and {100} growth sectors; also, cracks were often observed in the bulk of the growing crystals, the cracking probability being increased with increasing solution supersaturation.

The method allowed one to grow single crystals of $Cs_2Ni(SO_4)_2\cdot 6H_2O$ of up to $35\times 30\times 15$ mm dimensions; most crystals contained the bulk defects mentioned above.[87,88] A study of the crystal habit of $Cs_2Ni(SO_4)_2\cdot 6H_2O$ revealed a higher anisotropy of the normal growth rates ($R_{[100]}:R_{[010]}:R_{[001]}\approx 2.3:2:1$) compared to $(NH_4)_2Ni(SO_4)_2\cdot 6H_2O$, $K_2Ni(SO_4)_2\cdot 6H_2O$ and $Rb_2Ni(SO_4)_2\cdot 6H_2O$ crystals (Fig. ES.32).[79]

Crystals of $Cs_2Ni(SO_4)_2\cdot 6H_2O$ grown by cooling the solution contained inclusions of mother solution and, often, cracks (Fig. ES.33); this could be due to the presence of impurities.

The content of impurities in the starting salt and in the grown $Cs_2Ni(SO_4)_2\cdot 6H_2O$ crystals was analyzed by spark mass spectrometry taking the {110} growth sector as an example, because it is this sector that occupies the most part of the bulk of the crystal. The average effective impurity distribution coefficients (K_i) are listed in Table 14.

Table 14. Average effective impurity distribution coefficients for the {110} growth sector of $Cs_2Ni(SO_4)_2\cdot 6H_2O$ crystal.[94]

Impurity	K_i	Impurity	K_i
Li	0.3	Fe	1.0
K	2.2	Co	1.8
Rb	1.6	Cu	1.2
Mg	1.4	Si	2.0
Al	2.2	F	0.8
Ca	2.1	Cl	1.1
Cr	0.8	I	1.1

Since the K_i values of most impurities (Si, K, Rb, Ca, Mg, Al, Co and Cu) appeared to be larger than unity, these impurities were preliminarily removed from the starting solution by partial recrystallization. Subsequent chemical analysis of the grown $Cs_2Ni(SO_4)_2\cdot 6H_2O$ crystals revealed a considerable decrease in the content of Rb, K, Al, Ca, Co and Si as well as a some decrease in the concentrations of Mg, Cu and I.[94]

Nevertheless, in spite of preliminary purification of solutions, $Cs_2Ni(SO_4)_2\cdot 6H_2O$ crystals grown by cooling the solution still contained internal cracks. In another series of experiments,[91,94] crystal growth was carried out in isothermal conditions and the solution supersaturation was maintained by condensate takeoff. It this case, the solution supersaturation could be increased to ~1.5% without 'parasitic' spontaneous nucleation and emergence of cracks in the growing crystals. The normal growth rates along the [100], [010] and [001] directions were as high as 2.4, 2.8 and 1.1 mm day^{-1}, respectively.

To confirm the benefits of isothermal growth, the real structures of the $Cs_2Ni(SO_4)_2\cdot 6H_2O$ crystals grown by cooling the solution and under isothermal conditions from solutions with pH 3.5 were studied.

A photograph of the (001) cut and an X-ray projection topograph of a $Cs_2Ni(SO_4)_2\cdot 6H_2O$ crystal grown by cooling the solution are presented in Fig. 16. The presence of well-defined tilt sectorial boundaries (SB) is indicative of significantly different lattice constants of the {010}, {100} and {110} growth sectors along the diffraction vector due to nonuniform impurity distribution in different growth sectors.

Sharp kinks and bends in the images of sectorial boundary planes characterize multiple changes in the ratio of the growth rates of the neighbouring sectors. This can be explained by 'poisoning' of elementary growth steps on crystal faces by adsorbed impurity atoms (Cabrera–Vermilyea fence), because monotonic cooling of the solution was accompanied by a nonlinear dependence of the normal growth rates of crystal faces on time up to cessation of growth. As the solution supersaturation exceeded a critical value, σ^*, the elementary steps broke through the impurity fence to form macrosteps and the leading dislocation hillocks changed their geometry and dislocation hillocks interchange occurred.

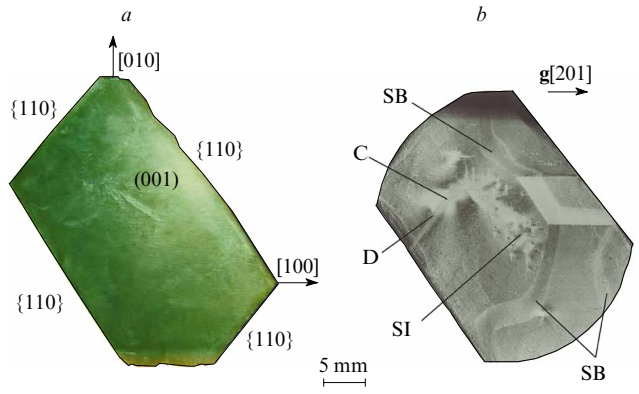


Figure 16. A photograph (*a*) and an X-ray projection topograph (*b*) of the (001) cut of $Cs_2Ni(SO_4)_2 \cdot 6H_2O$ crystal.[91]
For notations, see text.

Both the X-ray topograph and the optical image demonstrate clearly seen groups of cracks (C) formed on the solution inclusions (SI) due to the formation of macrosteps in the central part of the crystal. Also, dislocation bundles (D) appeared on cracks.[91, 94]

The (001) cut of the isothermally grown $Cs_2Ni(SO_4)_2 \cdot 6H_2O$ crystal and its X-ray projection topograph obtained by Lang X-ray projection topography are shown in Fig. 17.

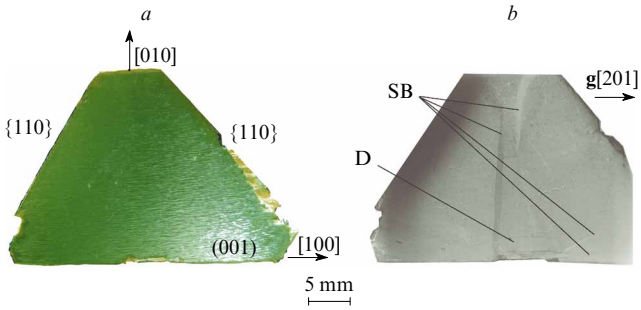


Figure 17. The (001) cut of a $Cs_2Ni(SO_4)_2 \cdot 6H_2O$ crystal grown at constant temperature.[91]
The sample (*a*) and X-ray projection topograph (*b*).

The real structure of this crystal differs from that of the crystal grown by cooling the solution (see Fig. 16). The crystal grown by removal of condensate is crack-free; sectorial boundaries demonstrate a lower contrast except the boundaries between the {010} and {110} growth sectors; therefore, the crystal is characterized by smaller differences between the lattice constants. The shape of sectorial boundaries points to small variations of the growth rate ratios for the neighbouring sectors. The X-ray projection topograph demonstrates individual dislocations propagating throughout the crystal from the seed region. No new emergence of dislocations was observed in the course of crystal growth.[91, 94]

However, almost all $Cs_2Ni(SO_4)_2 \cdot 6H_2O$ crystals grown in this series of experiments contained small inclusions of mother solution, mainly along the [201] direction; this had to influence the optical properties of the crystals. A study was carried out of the influence of the solution pH on the structural perfection of $Cs_2Ni(SO_4)_2 \cdot 6H_2O$ crystals because this parameter has strong effect on the forms of existence of inorganic impurities.[95]

Two methods described above were used to grow $Cs_2Ni(SO_4)_2 \cdot 6H_2O$ crystals from solutions with pH varied from 5.5 to 1.5; the saturation temperature was 48 °C. The filtered starting solution was acidified with sulfuric acid to pH 5.5, 4.5, 3.5, 2.5 and 1.5.[92] The photographs of these crystals are shown in Fig. ES.34.

Changes in pH of mother solution caused changes in the ratios of the growth rates of individual habit-forming crystal faces. This in turn led to changes in the relative size of particular faces up to their disappearance. For instance, the {100} and {010} pinacoid faces constitute the habit of the crystals grown from solutions with pH 5.5 and degenerate to edges for the crystals grown from more acidic solutions. On the contrary, the surface areas of the {110} and {011} faces of the rhomboid prism monotonically increase as pH of mother liquors increases.[92, 94] The average normal growth rates of selected faces of $Cs_2Ni(SO_4)_2 \cdot 6H_2O$ crystals are listed in Table 15, which also presents information on the presence of visible defects in the crystals at different solution pH. As can be seen, an increase in solution pH from 2.5 causes a slight decrease in the $R_{[100]}$ rate of $Cs_2Ni(SO_4)_2 \cdot 6H_2O$ crystals grown by both methods but has little effect on the normal growth rates along the [010] and [001] directions. Besides, crystal growth in more or less acidic solutions (relative to pH 2.5) is followed by the formation of visible structural defects in the growing crystals; the most defect structures were those of the samples grown from the starting solutions with pH 5.5.[94]

The influence of solution pH on the formation of inclusions in the growing $Cs_2Ni(SO_4)_2 \cdot 6H_2O$ crystals is in good agreement with the results of studies on their spectroscopic parameters (Fig. 18). It was found that the UV transmittance depends strongly on the mother solution pH, namely, the maximum transmittance (up to 90%) is characteristic of the samples grown from the solutions with pH 2.5, whereas the minimum transmittance (~70%) is

Table 15. Characteristics of $Cs_2Ni(SO_4)_2 \cdot 6H_2O$ crystals grown under different conditions.[94]

pH	Presence of visible defects	$R_{[100]}$	$R_{[010]}$	$R_{[001]}$
1.5	Small solution inclusions	1.7 / 1.8	1.8 / 1.6	0.6 / 0.6
2.5	No	1.7 / 1.8	1.8 / 1.7	0.6 / 0.6
3.5	Small solution inclusions	1.6 / 1.5	1.8 / 1.3	0.6 / 0.5
4.5	Solution inclusions	1.3 / 1.5	1.7 / 1.7	0.6 / 0.6
5.5	Cracks, solution inclusions	1.2 / 1.1	1.5 / 1.7	0.5 / 0.7

Note. Numbers in the numerator and in the denominator represent the growth rates of crystal faces (in mm day^{-1}) for crystals grown by lowering the temperature and by removal of condensate, respectively.

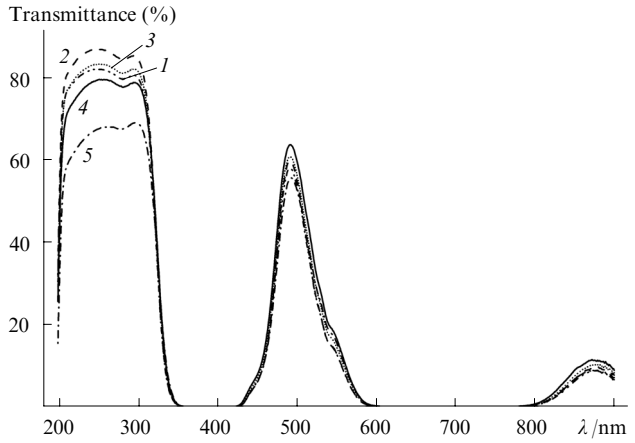


Figure 18. Transmission spectra of solution-grown $Cs_2Ni(SO_4)_2 \cdot 6H_2O$ crystals.
Solution pH: 1.5 (*1*), 2.5 (*2*), 3.5 (*3*), 4.5 (*4*), 5.5 (*5*).[94]

typical of the samples grown from the solutions with pH 5.5.[94]

The results of these investigations serve a basis for the method[94] and patent[96] for rapid growth of $Cs_2Ni(SO_4)_2 \cdot 6H_2O$ crystals of up to $120 \times 140 \times 55$ mm dimensions, with an average mass of up to 400 g, containing no visible defects (Fig. ES.35).[94,96] The average normal growth rates, R_x, R_y and R_z, of crystal faces were 2.4, 2.8 and 1.1 mm day^{-1}, respectively.

The $K_2Co(SO_4)_2 \cdot 6H_2O$ crystal. Crystals of $K_2Co(SO_4)_2 \cdot 6H_2O$ were for the first time grown[59] from solutions whose composition on the solubility curve of the $M^I_2M^{II}(SO_4)_2 \cdot 6H_2O$ salt was equidistant from two eutonic points; the concentration of cobalt was twice as high as the stoichiometric value. Crystal growth was carried out by cooling the solutions (cooling rate was at most 0.02 °C day^{-1}) under low supersaturations. The optical properties and structural perfection of crystals were not studied.

Pioneering experiments on the growth of $K_2Co(SO_4)_2 \cdot 6H_2O$ crystals were followed by a series of studies reported by another research group (see Refs 84, 93, 94 and 97), who used the starting solutions with pH 5.0 – 5.5 and low supersaturations (0.8% – 1.0%). The average normal growth rates, R_x, R_y and R_z, of crystal faces were 0.5, 0.65 and 0.4 mm day^{-1}, respectively. However, crystal growth was often accompanied by secondary nucleation and growth of 'parasitic' crystals. In most cases, crystals contained solution inclusions, mainly in the {010}, {100} and {201} growth sectors. Eventually, single crystals of up to $35 \times 50 \times 25$ mm dimensions along the principal crystallographic axes were grown (Fig. ES.36).[93]

Chemical analyses (see Table 16) of the $K_2Co(SO_4)_2 \cdot 6H_2O$ crystals grown from solutions purified by partial recrystallization revealed a considerable decrease in the concentrations of Rb, Ca, Ni, Mn, Zn and Si impurities and some decrease in the content of Mg, Cu and Al.

To study how the solution pH influences the formation of visible defects in $K_2Co(SO_4)_2 \cdot 6H_2O$ crystals, a series of single crystals were grown from solutions with pH in the range from 1.5 to 5.5.[84,94,97] The qualitative results are as follows:[94]

Table 16. Impuriy concentrations in the {010} growth sectors of $K_2Co(SO_4)_2 \cdot 6H_2O$ crystals.[94]

Impurity	Impurity concentration (10^{-4} mass %)					
	'as is' solution			after recrystallization in the temperature interval 50 – 45 °C		
Rb	5.0	5.2	4.8	3.3	3.5	3.6
Mg	2.4	2.6	2.4	2.2	2.0	2.0
Al	0.5	0.5	0.7	0.6	0.5	0.7
Ca	10.0	8.8	9.2	7.0	6.5	6.8
Cr	0.6	0.8	0.5	1.2	1.4	1.0
Fe	0.6	0.8	0.8	0.8	0.5	0.8
Ni	10.0	10.8	12.0	6.8	8.0	6.5
Cu	1.1	1.1	1.2	0.8	1.0	0.8
Mn	0.6	0.8	0.6	0.4	0.6	0.4
Zn	6.0	4.8	5.2	4.5	4.0	4.3
Si	10.0	10.0	11.0	7.8	7.6	7.4
F	1.0	1.2	1.4	1.0	1.5	1.2
Cl	4.0	4.2	3.8	3.8	3.5	3.6
I	0.6	0.5	0.6	0.8	0.6	0.8

pH 1.5 — small solution inclusions are present in the {010} growth sector;

pH 2.5 — almost no defects;

pH 3.5 — small solution inclusions are present in the {010} growth sector;

pH 4.5 — small solution inclusions are present in the {100} and {010} growth sectors;

pH 5.5 — extended solution inclusions are present in the {100}, {010} and {201} growth sectors.

The characteristic inclusions in these crystals are shown in Fig. ES.37.

Thus, like for $Cs_2Ni(SO_4)_2 \cdot 6H_2O$, the growth of $K_2Co(SO_4)_2 \cdot 6H_2O$ crystals in either more or less acidic solutions (relative to pH 2.5) is followed by the formation of visible solution inclusions in the growing crystals. The concentration and size of defects, as well as the number of growth sectors containing these defects increase with increasing solution pH.

To confirm the effect of solution pH on the optical properties of the crystals grown, their spectral characteristics were studied in the 200 – 900 nm wavelength range (Fig. 19).[84,97] As was expected, the results obtained demonstrate the dependence of transparency and, consequently, structural perfection, of the crystals on the solution pH. The maximum UV transmittance (> 80%) was observed for the crystals grown from the solutions with pH 2.3; an increase in pH to 5.5, as well as a decrease to pH < 2.5 causes the transmittance in both spectral intervals to decrease.[94]

Different degrees of structural perfection of the samples grown at different pH can be explained by the influence of solution pH on the forms of existence of inorganic impurities in the solution; this was described in detail[95] taking potassium dihydrogenphosphate solutions as examples. At high solution pH values, impurities block kinks in the growth steps, which then leads to formation of scattering centres, *viz.*, inclusions.[98]

The kinetic curve for growth of $K_2Co(SO_4)_2 \cdot 6H_2O$ crystals is shown in Fig. ES.38. The blocking action of impurities ceases at supersaturations of 1.8% – 2.0%. This corresponds to rare formation of visible defects in crystals

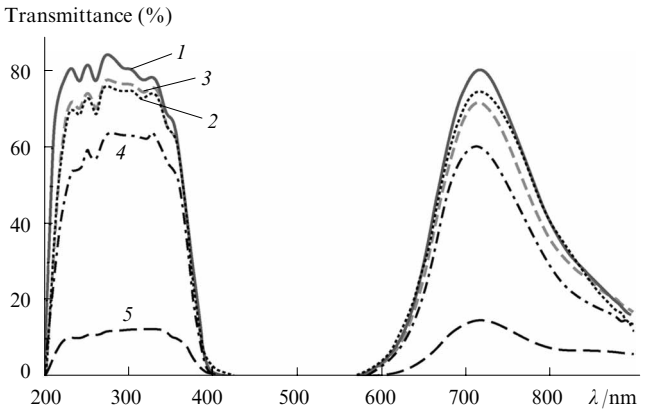


Figure 19. Transmission spectra of solution-grown $K_2Co(SO_4)_2 \cdot 6H_2O$ crystals.
Solution pH: 2.3 (*1*), 2.9 (*2*), 3.5 (*3*), 4.1 (*4*), 5.5 (*5*).[97]

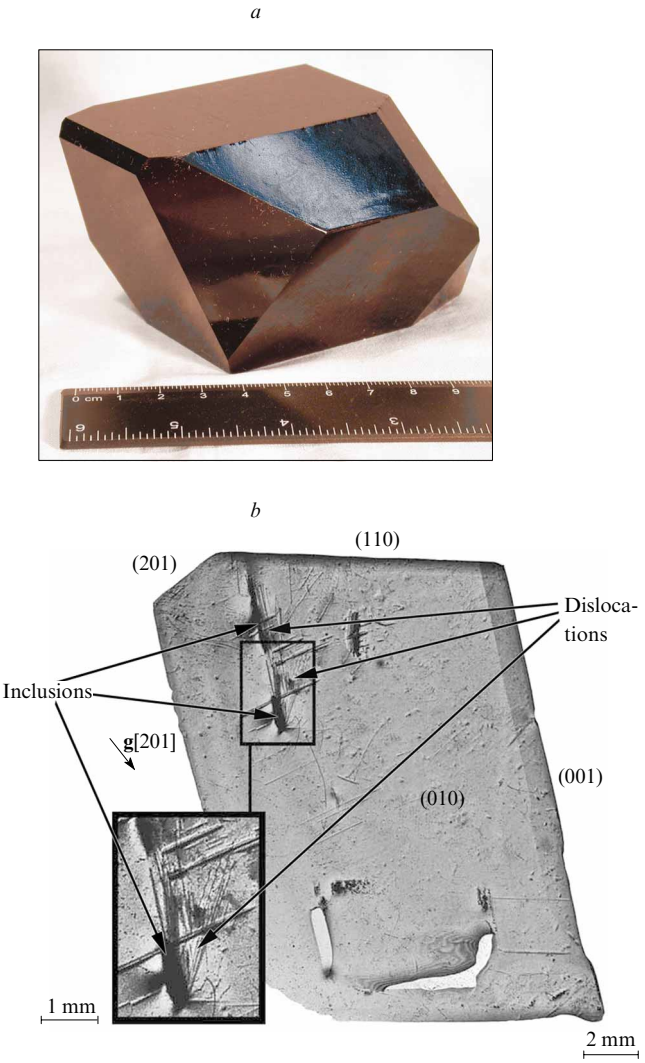


Figure 20. A photograph (*a*)[94] and an X-ray topograph (*b*)[97] of $K_2Co(SO_4)_2 \cdot 6H_2O$ crystal.

at solution velocities of $\sim 15-20$ cm s^{-1} near the surface of the growing faces and the average normal growth rates, R_x, R_y and R_z, of crystal faces were 0.8, 1.0, 0.5 mm day^{-1}, respectively.

Almost all experiments carried out under higher supersaturations were accompanied by secondary nucleation. The $K_2Co(SO_4)_2 \cdot 6H_2O$ crystals grown in 5-litre crystallizers had average dimensions of $95 \times 115 \times 40$ mm along the principal crystallographic axes, the maximum mass of crystals was 530 g; the average growth duration was 70 days.[94] The photograph and X-ray topograph of the $K_2Co(SO_4)_2 \cdot 6H_2O$ crystal are shown in Fig. 20.

The upper left region of the topograph demonstrates individual solution inclusions on which dislocation bundles appear. These inclusions were formed near the hypothetical boundary between the {201} and {110} growth sectors, where they can be trapped with higher probability. Besides, a few small solution inclusions were found in the region of seed regeneration. The fact that no X-ray diffraction contrast was observed at sectoral boundaries indicates a uniform impurity distribution between the growth sectors in the crystal. No zonal inhomogeneities were also observed. An investigation of the defect structure of the $K_2Co(SO_4)_2 \cdot 6H_2O$ crystal grown in this temperature regime revealed a reasonably high structural perfection.

III.6. Thermal stability of $M^I_2M^{II}(SO_4)_2 \cdot 6H_2O$ crystals

Studies on the thermal stability of $K_2Ni(SO_4)_2 \cdot 6H_2O$ crystals grown from solutions acidified with hydrochloric acid were reported.[10,14] The dehydration temperature of $K_2Ni(SO_4)_2 \cdot 6H_2O$ was found to be 97 °C [10] and 110 °C (at a sample heating rate of 5 °C min^{-1}).[14]

In the text above we discussed the influence of various factors on the processes occurring on heating, including the dehydration temperature. Since conditions of TGA experiments [10,14] were not specified, the results obtained seem not to be reliable and reproducible.

The thermal stability of $(NH_4)_2Ni(SO_4)_2 \cdot 6H_2O$ crystal was studied.[11,15] The dehydration temperature of the crystal was reported as 96 °C;[11] however, the experimental conditions including the heating rate were not specified, like in Refs 10 and 14.

Thermal stability studies of polycrystalline $K_2Ni(SO_4)_2 \cdot 6H_2O$ and $K_2Co(SO_4)_2 \cdot 6H_2O$ samples (grain size in the range $130-170$ μm, heating rate of 1.5 °C min^{-1}) gave a dehydration temperature of 95 and 87 °C, respectively.[99]

Experiments [15] on the determination of the dehydration temperatures of α-$NiSO_4 \cdot 6H_2O$, $(NH_4)_2Ni(SO_4)_2 \cdot 6H_2O$ and $K_2Ni(SO_4)_2 \cdot 6H_2O$ crystals were carried out in different conditions. Optical UV filters (α-$NiSO_4 \cdot 6H_2O$, $K_2Ni(SO_4)_2 \cdot 6H_2O$ and $(NH_4)_2Ni(SO_4)_2 \cdot 6H_2O$) had the same geometry, underwent identical mechanical treatment and were placed in a quartz ampoule. The ampoule was evacuated to 600 mm Hg, sealed, placed into an oven and heated to 50 °C. Then, the ampoule was heated from 50 to 140 °C with an increment of 5 °C, being kept at each temperature for 72 h. The dehydration temperatures (T_{dehydr}) determined in this experiment were as follows:

Crystal	T_{dehydr}/°C
α-$NiSO_4 \cdot 6H_2O$	70
$K_2Ni(SO_4)_2 \cdot 6H_2O$	105
$(NH_4)_2Ni(SO_4)_2 \cdot 6H_2O$	135

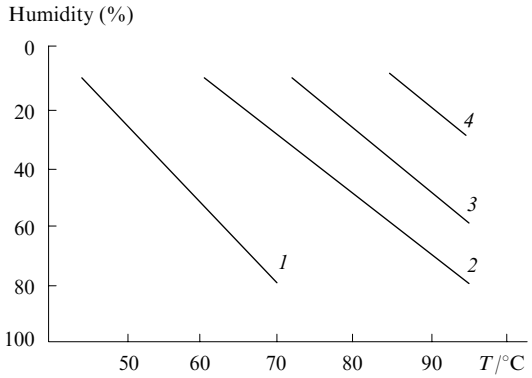


Figure 21. Stability regions of compounds in the temperature–humidity coordinates.[15]
Compound: $Ni(SO_4)_2 \cdot 6H_2O$ (*1*), $NiSiF_6 \cdot 6H_2O$ (*2*), $K_2Ni(SO_4)_2 \cdot 6H_2O$ (*3*) and $(NH_4)_2Ni(SO_4)_2 \cdot 6H_2O$ (*4*).

Then, optical UV filters were tested in a climate chamber in the temperature- and humidity-programmed regime. The results obtained are presented in Fig. 21 in the form of lines representing the boundaries of thermal stability for each compound. The slopes of the lines corresponding to the three different crystals are rather close; the thermal stability of $(NH_4)_2Ni(SO_4)_2 \cdot 6H_2O$ is the highest among the crystals studied.

In the last stage of the research only the thermal stability of an $(NH_4)_2Ni(SO_4)_2 \cdot 6H_2O$ element was tested. The conditions of the experiment were as close as possible to those in a sealed UV filter. In a closed system, the $(NH_4)_2Ni(SO_4)_2 \cdot 6H_2O$ crystal was stable up to 125 °C over a period of two weeks.[15]

III.7. Correlations between structural features of $M^I_2Ni(SO_4)_2 \cdot 6H_2O$ and $M^I_2Co(SO_4)_2 \cdot 6H_2O$ crystals and dehydration temperature

The thermal stability of $M^I_2Ni(SO_4)_2 \cdot 6H_2O$ crystals was studied by DTA and TGA.[80, 93, 94] Of particular interest are the experimentally found nonlinear changes in the dehydration temperature of compounds belonging to the nickel series of Tutton's salts, namely, $K_2Ni(SO_4)_2 \cdot 6H_2O$, $Rb_2Ni(SO_4)_2 \cdot 6H_2O$ and $Cs_2Ni(SO_4)_2 \cdot 6H_2O$.

Taking into account the availability of a rather large array of structural data and correctly measured thermal stability values of the $M^I_2Ni(SO_4)_2 \cdot 6H_2O$ (M^I = K, Rb, Cs) crystals, one can carry out a comparative analysis of their structures in order to find correlations between certain structural features and changes in the dehydration temperatures within this isotypic series.

As mentioned above, the structures of these crystals represent frameworks of complex octahedral cations $[Ni(H_2O)_6]^{2+}$ located at inversion centres and hydrogen-bonded to tetrahedral anions $[SO_4]^{2-}$. Alkali metal cations are located inside the frameworks in the $[M^+O_8]$ polyhedra of irregular shape. The size of the polyhedron increases with the ionic radius of the cation, thus leading to an increase in the unit cell volume of $Rb_2Ni(SO_4)_2 \cdot 6H_2O$ and $Cs_2Ni(SO_4)_2 \cdot 6H_2O$ crystals compared to that of $K_2Ni(SO_4)_2 \cdot 6H_2O$ by 4.2% and 10.4%, respectively.

An expansion of the $[M^+O_8]$ polyhedron causes displacements and rotation of the $[SO_4]^{2-}$ tetrahedra and subsequent changes in the length and direction of the hydrogen bonds between oxygen atoms of the tetrahedron and octahedron (Table 17). This in turn influences the size and shape of the $[Ni(H_2O)_6]^{2+}$ octahedron (Fig. 22). As the ionic radius of the alkali metal increases, the hydrogen bonds involving the O(5) and O(7) oxygen atoms of the octahedron elongate, the O(1)–O(5)–O(3) and O(2)–O(7)–O(4) angles decrease, whereas the hydrogen bonds involving the O(6) atom shorten and the O(1)–O(6)–O(2) angle simultaneously increases. Within the octahedron, the distances between the Ni atom and O(5) atom elongate and the distances between the Ni atom and O(6) atoms shorten. Thus, an expansion of the $[M^+O_8]$ polyhedron leads to contraction of the $[Ni(H_2O)_6]^{2+}$ octahedron along the O(6)–O(6) direction and to its extension along the O(5)–O(5) direction.

Table 17. Selected structural parameters of $Cs_2Ni(SO_4)_2 \cdot 6H_2O$ (I), $Rb_2Ni(SO_4)_2 \cdot 6H_2O$ (II) and $K_2Ni(SO_4)_2 \cdot 6H_2O$ (III) crystals.

Parameter	I (see [79])	II (see [80])	III (see [74])
Effective ionic radius of M^{1+} cation /Å	1.67 [a]	1.52 [a]	1.38 [a]
Unit cell volume /Å^3	718.4	677.6	650.56(8)
Complex cation $[Ni(H_2O)_6]^{2+}$			
Distance /Å			
Ni–O(5) × 2	2.0329(14)	2.0227(20)	2.0205(13)
Ni–O(6) × 2	2.0596(13)	2.0672(17)	2.0758(13)
Ni–O(7) × 2	2.0796(16)	2.0781(22)	2.0850(12)
Angle /deg			
O(5)–Ni–O(6)	89.167(72)	89.722(78)	89.55(6)
O(5)–Ni–O(7)	89.149(76)	89.641(82)	89.89(6)
O(6)–Ni–O(7)	88.501(68)	88.351(77)	88.39(5)
Hydrogen bond O(*octahedron*)···O(*tetrahedron*)			
Distance /Å			
O(5)–O(1)	2.7566(20)	2.7398(28)	2.7253(18)
O(5)–O(3)	2.6819(19)	2.671(3)	2.6606(16)
O(6)–O(1)	2.7401(19)	2.7516(25)	2.7858(19)
O(6)–O(2)	2.7835(23)	2.7929(29)	2.8157(20)
O(7)–O(2)	2.7551(20)	2.7416(30)	2.7441(18)
O(7)–O(4)	2.7219(18)	2.6971(23)	2.6706(16)
Hydrogen bonds O(*tetrahedron*)···O(*octahedron*)···O(*tetrahedron*)			
Angle /deg			
O(1)···O(5)···O(3)	94.134(82)	97.800(86)	101.668(68)
O(2)···O(6)···O(1)	116.807(78)	115.442(83)	113.613(62)
O(4)···O(7)···O(2)	99.423(84)	102.192(95)	103.622(74)
$[M^+–O(8)]$ *Polyhedron*			
Distance /Å			
M^+–O(1)	3.0542(13)	2.8687(18)	2.7264(14)
M^+–O(2)	3.0871(11)	2.9326(16)	2.8111(14)
M^+–O(3)	3.1108(16)	2.9887(17)	2.9092(16)
M^+–O(3)	3.0947(13)	2.9781(21)	2.8859(16)
M^+–O(4)	3.2683(14)	3.1391(21)	2.9625(19)
M^+–O(4)	3.3153(16)	3.2159(23)	3.2562(19)
M^+–O(6)	3.4204(15)	3.2247(19)	3.1078(14)
M^+–O(7)	3.3049(17)	3.1151(21)	2.9652(14)

[a] The efffective ionic radii were taken from Ref. 81.

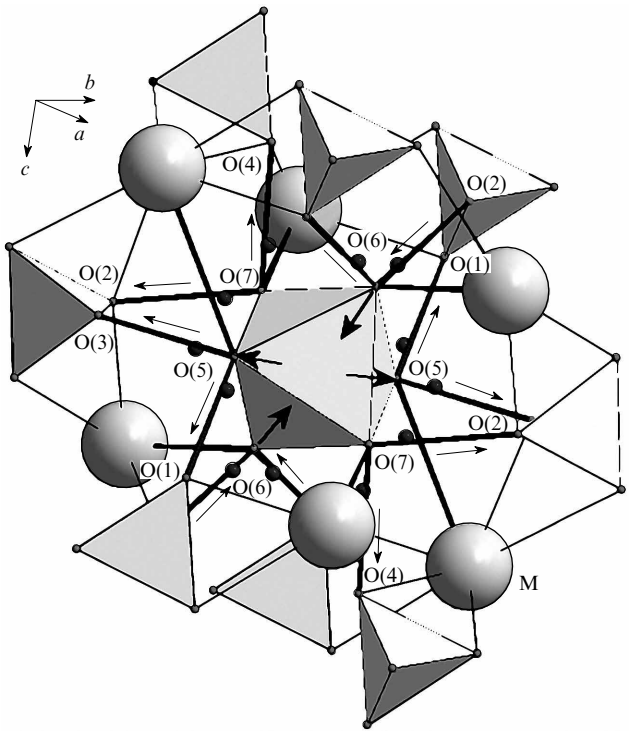


Figure 22. The nearest environment of $[Ni(H_2O)_6]^{2+}$ octahedron.[80] Arrows show how the bond lengths change with increasing ionic radius of the alkali metal M = Cs, Rb, K.

An increase in the radius of the alkali cation causes nonmonotonic changes in the length of the diagonal of the nickel octahedron along the O(7) – Ni – O(7) direction, namely, this distance is the longest for $K_2Ni(SO_4)_2 \cdot 6H_2O$ and the shortest for $Rb_2Ni(SO_4)_2 \cdot 6H_2O$. The character of changes in this distance correlates with the pattern of changes in the thermal stability of crystals of the nickel series of Tutton's salts. This can be explained by the fact that the O(7) atoms belong to two water molecules that are the most distant from the nickel ion and are eliminated first on heating the crystal. Thus, shortening of the O(7) – Ni – O(7) distances in the isotypic series $K_2Ni(SO_4)_2 \cdot 6H_2O - Cs_2Ni(SO_4)_2 \cdot 6H_2O - Rb_2Ni(SO_4)_2 \cdot 6H_2O$ corresponds to enhancement of the thermal stability of crystals.

A similar analysis was performed[94] for compounds belonging to the cobalt series of Tutton's salts ($M^I_2Co(SO_4)_2 \cdot 6H_2O$). The dehydration temperatures of the $M^I_2Co(SO_4)_2 \cdot 6H_2O$ (M^I = K, Rb, Cs) crystals were determined and a correlation between their thermal stabilities and the Co – O(6) distance was analyzed {O(6) are the oxygen atoms of two water molecules that are the most distant from the cobalt ion in the $[Co(H_2O)_6]^{2+}$ octahedron}. It was found that the thermal stability of crystals from the cobalt series of Tutton's salts also depends on the Co – O(6) distance (Table 18). Correlations between the thermal stabilities of the $M^I_2Ni(SO_4)_2 \cdot 6H_2O$ and $M^I_2Co(SO_4)_2 \cdot 6H_2O$ crystals and the Ni – O(7) and Co – O(6) distances are illustrated in Fig. 23.

Summing up, an analysis of the results obtained in studies of the crystal structure of nickel-containing Tutton's salts showed that nonmonotonic changes in the thermal

Table 18. Dehydration temperatures of $M^I_2Co(SO_4)_2 \cdot 6H_2O$ crystals and Co – O distances in the $[Co \cdot 6H_2O]$ octahedron.[94]

Crystal	T_{dehydr} /°C (see [a])	Co – O distances in the $[Co \cdot 6H_2O]^{2+}$ octahedron /Å		
		see [b]	see [c]	see [d]
$K_2Co(SO_4)_2 \cdot 6H_2O$	47	2.0391(13)	2.1215(13)	2.1369(13)
$Rb_2Co(SO_4)_2 \cdot 6H_2O$	49	2.0485(20)	2.1103(17)	2.1220(22)
$Cs_2Co(SO_4)_2 \cdot 6H_2O$	51	2.0677(20)	2.1051(20)	2.1196(18)

[a] Single-crystalline samples were heated at a rate of 0.12 °C min^{-1}; [b] [Co – O(7)] × 2; [c] [Co – O(5)] × 2; [d] [Co – O(6)] × 2.

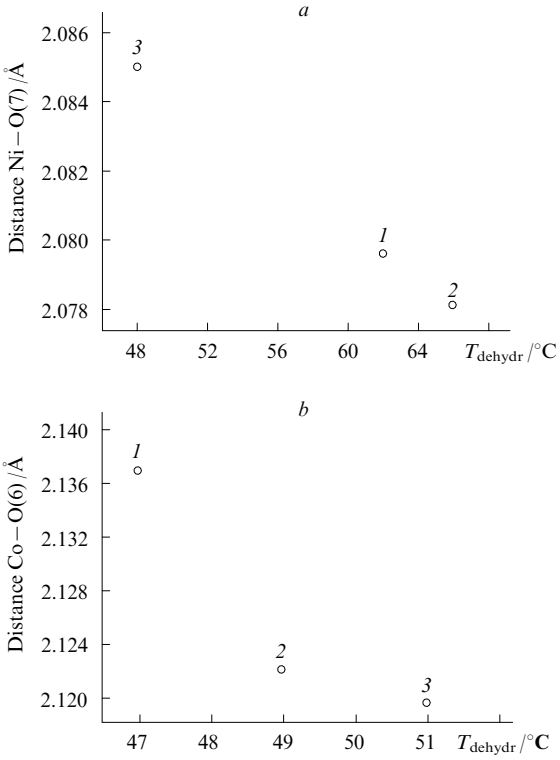


Figure 23. Correlations between the thermal stability of $M^I_2M^{II}(SO_4)_2 \cdot 6H_2O$ crystals and the M^{II} – O distance.[94] M^{II} = Ni (*a*), Co (*b*); M^I: Cs (*1*), Rb (*2*) and K (*3*); O is an oxygen atom from two most distant (relative to the M^{II} atom) water molecules.

stability within the series $K_2Ni(SO_4)_2 \cdot 6H_2O - Rb_2Ni(SO_4)_2 \cdot 6H_2O - Cs_2Ni(SO_4)_2 \cdot 6H_2O$ are due to nonmonotonic changes in the distance between the Ni^{2+} cation and two most distant bound water molecules of the $[Ni(H_2O)_6]^{2+}$ octahedron. Studies on the thermal stability and structural features of cobalt-containing Tutton's salts ($M^I_2Co(SO_4)_2 \cdot 6H_2O$) confirmed this correlation.

IV. Conclusion

The properties of crystals of α-$NiSO_4 \cdot 6H_2O$ and nickel-containing Tutton's salts have been studied in quite detail. Methods for crystal growth were developed and the crystal structure, transmission spectra and thermal stability were

investigated. This is also valid for the $K_2Co(SO_4)_2 \cdot 6H_2O$ crystal and to a lesser extent for crystals of other compounds belonging to the cobalt family of Tutton's salts. In particular, the results obtained allow one to establish a correlation between the structural parameters of the crystals and the dehydration temperature.

Based on the spectroscopic parameters, all these crystals are suitable for application as UV filters. Considering a combination of the optical properties, thermal stability and processability, α-$NiSO_4 \cdot 6H_2O$, $Cs_2Ni(SO_4)_2 \cdot 6H_2O$ and $K_2Co(SO_4)_2 \cdot 6H_2O$ seem to be the most promising crystals. Currently, they are efficiently used in practice and provide high operating parameters of devices.

At the same time, researchers continue their efforts to find novel materials for UV optical filters. The research directions include enhancement of the thermal stability of crystals and the efficiency of UV filtration in order to extend the scope of application of the solar-blind technology.

Usually, the dehydration temperatures of the practically utilized crystals are at most 100 °C. However, a number of applications require an increase in the upper operating temperature to 120 °C. In turn, an increase in the optical density of crystals beyond the operating wavelength range (provided a necessary transparency level in the operating spectral range) will allow one to decrease the mass and dimensions of devices and thus significantly extend the field of their application. The case in point is that the presence of 'parasitic' transmission bands of a crystalline filter forces engineers to design optical paths containing a large number of auxiliary elements (interference filters, diaphragms, mirrors) in order to reduce the background. Improved efficiency of optical filtration will significantly simplify the design of solar-blind lenses and reduce their dimensions and mass.

In this respect, there are scarce communications on the growth and investigation of crystals belonging to other classes of compounds, in particular, $Na_2Ni(SO_4)_2 \cdot 4H_2O$ (see Ref. 100) and $Ni(BF_4)_2 \cdot 6H_2O$.[101] It was stated that dehydration of both crystals begins at temperatures above 100 °C. The transmission spectrum of the $Na_2Ni(SO_4)_2 \cdot 4H_2O$ crystal almost exactly matches that of $(NH_4)_2Ni(SO_4)_2 \cdot 6H_2O$, whereas the transmittance of the $Ni(BF_4)_2 \cdot 6H_2O$ crystal at about 250 and 480 nm is nearly the same, being equal to ~40%. Probably, in the latter case one deals with a consequence of low structural perfection of the sample.

However, most studies are devoted to growth of crystals of solid solutions (mixed crystals) or compounds of nickel sulfates and other divalent metals. One of the first studies in this field concerns $FeNi(SO_4)_2 \cdot 12H_2O$ crystals (T_{dehydr} = 80 °C).[102] Also, $Ni_xZn_{1-x}SO_4 \cdot 7H_2O$ crystals were described; however, no TGA measurements were performed.[103, 104] Crystals $K_2Mg_xNi_{1-x}(SO_4)_2 \cdot 6H_2O$ with T_{dehydr} of up to 110 °C were investigated.[105–107] For all these crystals, the introduction of an extra cation M^{2+} leads to enhanced transmittance in the vicinity of λ = 480 nm up to values comparable with the UV transmittance.

As to the growth of crystals of solid solutions, growth of mixed crystals of compounds containing Ni^{2+} and Co^{2+} ions seems to be the most promising investigation line. In this case, the transmission band of nickel salts in the visible region in the vicinity of λ = 480 nm is weakened due to superimposition of the absorption bands of the nickel and cobalt ions.

Crystals of $CoNi(SO_4)_2 \cdot 12H_2O$ ($T_{dehydr} \approx 85$ °C) were studied.[108] Owing to small thickness of the sample the transmission spectra were measured for aqueous salt solution. Transmittance in the visible region was found to be much lower compared to that of $NiSO_4 \cdot 6H_2O$ solution.

An $(NH_4)_2Co_{0.17}Ni_{0.83}(SO_4)_2 \cdot 6H_2O$ crystal ($T_{dehydr} \approx$ 97 °C) was grown and studied.[109] Its transmittance in the vicinity of λ = 480 nm was nearly halved, but the UV transmittance decreased by ~25%; this indicates a structural perfection of the crystal.

The growth and investigation of the properties of $K_2Co_xNi_{1-x}(SO_4)_2 \cdot 6H_2O$ crystals of different composition was described.[110–112] The transmittance in the visible region decreased, but the UV transmittance was at most 40% even for samples 1–2 mm thick, thus indicating high defectiveness of the samples. The $K_2Co_{0.1}Ni_{0.9}(SO_4)_2 \cdot 6H_2O$ crystal was characterized by T_{dehydr} = 98 °C.[110]

Generally, solution-grown mixed crystals are characterized by enhanced defect formation. Owing to different types of incorporation of isomorphic components into the lattice, such crystals exhibit high zonal and sectorial inhomogeneity, high internal stress and usually contain cracks and a large amount of solution inclusions.

Besides, growth of crystals of binary solid solutions from aqueous solutions is complicated by the fact that, according to the Gibbs phase rule, the number of the degrees of freedom for such a system is two (temperature and composition provided that the pressure and volume are constant). If the chemical compositions of the solid and liquid phases do not meet the equilibrium condition specified by the phase diagram, various complex multidirectional processees (*e.g.*, simultaneous dissolution of the crystal and growth of a crystalline phase of some other composition) are possible in such systems. As a consequence, the crystal surface is transformed to a mosaic of randomly arranged spots of different composition.[113, 114] When mixed single crystals are grown, this can be due to local fluctuations of the solution composition owing to, *e.g.*, non-stationary convection. In this case, a new type of inhomogeneity termed mosaic 'microheterogeneity', which is atypical of single-component crystals, will be formed in the crystal.[115, 116]

These processes can be suppressed by creating (i) a particular supercooling in the system (to prevent dissolution and ensure only crystal growth)[114] and (ii) stable flow hydrodynamics. Taking into account these features, mixed crystals $K_2Co_xNi_{1-x}(SO_4)_2 \cdot 6H_2O$ were grown,[117] namely, rather large (up to 80 × 15 × 12 mm) optically perfect crystals of different composition. The UV transmittance of samples 1 cm thick was as high as 83%, being only 3% in the 400–600 nm wavelength range. The crystals were characterized by rather high internal stress due to nonuniform distribution of isomorphic components and were highly brittle. Main sources of stress include sectorial inhomogeneity[117] and a ~4-mm vicinity of the seed point where the concentrations of the isomorphic components change by 7 mass %–8 mass %.[110] X-Ray diffraction studies[118, 119] revealed no concentration anomalies in the distribution components in the crystal lattice, *viz.*, cobalt ions randomly replace nickel ions in the whole range of compositions. This offers hope that mixed crystals with improved optical properties for practical applications can be obtained by

optimizing the growth conditions. The dehydration temperature of these crystals is at most 100 °C, but their thermal stability is at least competitive with that of the presently available materials, while improved UV filtration parameters make them promising for practical applications.

The review has been written with the financial support from the Russian Science Foundation (RSF Project No. 15-12-00030).

References

1. D M Reilly, D T Moriarty, J A Maynard *Proc. SPIE Int. Soc. Opt. Eng.* **5611** 244 (2004)
2. P Sandvik, K Mi, F Shahedipour, R McClintock, A Yasan, P Kung *J. Cryst. Growth* **231** 366 (2001)
3. N Biyikli, I Kimukin, O Aytur, E Ozbay *IEEE Photon. Technol. Lett.* **16** 1718 (2004)
4. D Caputo, G Cesare, F Irrera, F Palma *IEEE Transact. Electron. Dev.* **43** 1351 (1996)
5. F Yan, X Xin, S Aslam, Y Zhao, D Franz, J Zhao, M Weiner *IEEE J. Quant. Electron.* **40** 1315 (2004)
6. A A Altukhov, A Yu Mityagin, A M Klochkova, G A Orlova *Tekhnol. Konstr. Elektron. Apparat.* (3) 3 (2008)
7. A A Altukhov, V V Gavrilov, V V Eremin, V A Kireev *Prikladnaya Fiz.* (2) 76 (2004)
8. V V Eremin *Bezopasnost' Truda v Promyshlennosti* (7) 36 (2006)
9. Y He, G Su, X Yu, Zh Li, B Huang, R Jang, Q Zhao *J. Cryst. Growth* **169** 193 (1996)
10. Y He, J Chen, G Su, X Zhuang, G Lee, J Rihong *J. Cryst. Growth* **233** 809 (2001)
11. G Su, X Zhuang, Y He, Zh Li, G Wang *J. Phys. D: Appl. Phys.* **35** 2652 (2002)
12. Patent China 1407143 (2002)
13. Patent China 99108240 (2000)
14. Patent US 5788765 (1998)
15. Patent US 6452189 (2002)
16. D T Sviridov, R K Sviridova, Yu F Smirnov *Opticheskie Spektry Ionov Perekhodnykh Metallov v Kristallakh* (Optical Spectra of Transition Metal Ions in Crystals) (Moscow: Nauka, 1976)
17. O N Boksha, S V Grum-Grzhimailo *Issledovanie Opticheskikh Spektrov Kristallov s Ionami Gruppy Zheleza pri Komnatnoi i Nizkikh Temperaturakh* (Investigation of Optical Spectra of Crystals with Iron Group Ions at Room and Low Temperatures) (Moscow: Nauka, 1972)
18. A Mookherji, N S Chhonkar *Indian J. Phys.* **42** 260 (1968)
19. A Chretien, R Rohmer *C.R. Acad. Sci.* **198** 92 (1934)
20. *Gmelins Handbuch der anorganischen Chemie. Nikel* System-Nr. 57, Teil B, Lfg. 2 (Weinheim: Verlag Chemie, 1966) S. 685
21. J W Mellor, in *A Comprehensive Treatise on Inorganic and Theoretical Chemistry* Vol. XV (London, New York, Toronto: Longmans Green and Co., 1936) p. 453
22. R Rohmer *C.R. Acad. Sci.* **201** 672 (1935)
23. A V Babajewa, E I Daniluschkina *Z. Anorg. Allg. Chem.* **226** 338 (1936)
24. J A Addlestone *J. Phys. Chem.* **42** 437 (1937)
25. C Beevers, H Lipson *Z. Kristallogr.* **83** 123 (1932)
26. B O'Connor, D Dale *Acta Crystallogr.* **21** 705 (1966)
27. K Stadnicka, A Glazer, M Koralewski *Acta Crystallogr., Sect. B* **43** 319 (1987)
28. L D Iskhakova, L S Dubrovinskii, I A Charushnikova *Sov. Phys. Crystallogr.* **36** 360 (1991) [*Kristallografiya* **36** 650 (1991)]
29. J Hester, E Maslen, A Glazer, K Stadnicka *Acta Crystallogr., Sect. B* **49** 641 (1993)
30. R Angel, L Finger *Acta Crystallogr., Sect. C* **44** 1869 (1988)
31. A A Sidel'nikov, A P Chupakhin, N Z Lyakhov, V V Boldyrev *Dokl. Akad. Nauk. SSSR* **258** 158 (1981)
32. A N Winchell, H Winchell *The Microscopical Characters of Artificial Inorganic Solid Substances: Optical Properties of Artificial Minerals* (New York: Academic Press, 1964)
33. K A Kaldybaev, A F Konstantinova, Z B Perekalina *Girotropiya Odnoosnykh Pogloshchayushchikh Kristallov* (Gyrotropy of Uniaxial Absorbing Crystals) (Moscow: Institute for Socio-Economic and Environmental Production and Investment Issues, 2000)
34. R Grinter, M Harding, S Mason *J. Chem. Soc. A* 667 (1970)
35. J Moxon, A Renshaw, I Tebbutt *J. Phys. D: Appl. Phys.* **24** 1187 (1991)
36. Y O Dovgii, I G Mankovskaya *Phys. Solid State* **40** 1460 (1998) [Ya O Dovgii, I G Man'kovskaya *Fiz. Tv. Tela* **40** 1608 (1998)]
37. F Cotton, G Wilkinson *Advanced Inorganic Chemistry* (New York, London: Wiley, 1962)
38. L Velluz, M Legrand, M Grosjean *Optical Circular Dichroism* (New York: Academic Press, 1965)
39. G Rabbering, J Wanrooy, A Schuijff *J. Thermochim. Acta* **12** 57 (1975)
40. M Friesen, H Burt, A Mitchell *J. Thermochim. Acta* **41** 167 (1980)
41. P Nandi, D Deshpande, V Kher *J. Thermochim. Acta* **32** 143 (1979)
42. J Thomas, G Renshaw *J. Chem. Soc. A* 2749 (1969)
43. J Thomas, G Renshaw *J. Chem. Soc. A* 2753 (1969)
44. J Thomas, G Renshaw *J. Chem. Soc. A* 2756 (1969)
45. N Koga, H Tanaka *J. Phys. Chem.* **98** 10521 (1994)
46. Yu N Makurin, E I Stepanovskikh, L A Brusnitsyna *Kinetika Slozhnykh Reaktsii: Uchebnoe Posobie* (The Kinetics of Complex Reactions: a Tutorial) (Ekaterinburg: UGTU – UPI, 2008)
47. G Su, Y He, Zh Li, R Jiang, Ch Zhu, Sh Yang *J. Cryst. Growth* **213** 99 (2000)
48. L V Soboleva, E B Rudneva, I L Smolsky *Crystallogr. Rep.* **43** 706 (1998) [*Kristallografiya* **43** 756 (1998)]
49. E B Rudneva, V L Manomenova, M V Koldaeva, D N Karimov, A E Voloshin III, in *Program and Abstract Book of International Conference 'Crystal Materials 2010', Kharkov, 2010* p. P65
50. V L Manomenova, E B Rudneva, A E Voloshin, in *Tezisy Dokladov XI Natsional'noi Konferentsii po Rostu Kristallov* (Abstracts of Reports of the XIth National Conference on Crystal Growth, Moscow, 2004) p. 269
51. V L Manomenova, E B Rudneva, A shch Voloshin, L V Soboleva, A B Vasil'ev, B V Mchedlishvili *Crystallogr. Rep.* **50** 877 (2005) [*Kristallografiya* **50** 937 (2005)]
52. K V Ravi *Imperfections and Impurities in Semiconductor Silicon* (New York: Wiley, 1981)
53. N Zaitseva, L Carman *Prog. Cryst. Growth Characterizat. Mater.* **43** 1 (2001)
54. A E Tutton *J. Chem. Soc. Trans.* **63** 337 (1893)
55. A E Tutton *J. Chem. Soc. Trans.* **69** 507 (1896)
56. A E Tutton *J. Chem. Soc. Trans.* **69** 495 (1896)
57. A Benrath *Z. Anorg. Allg. Chem. B* **208** 169 (1932)
58. R M Caven, W Johnston *J. Chem. Soc.* 2628 (1926)

59. L V Soboleva, L F Kirpichnikova *Crystallogr. Rep.* **46** 306 (2001) [*Kristallografiya* **46** 350 (2001)]
60. V Ya Anosov, S A Pogodin *Osnovnye Nachala Fiziko-Khimicheskogo Analiza* (Fundamentals of Physicochemical Analysis) (Moscow, Leningrad: Academy of Sciences of the USSR, 1947)
61. G Wollmann, W Voigt *J. Fluid Phase Equil.* **291** 154 (2010)
62. A E Hill, W J Taylor *J. Am. Chem. Soc.* **60** 1099 (1938)
63. L V Soboleva *Crystallogr. Rep.* **52** 1104 (2007) [*Kristallografiya* **52** 1141 (2007)]
64. H Wetzel, A Gumpers, J Koppel *Z. Phys. Chem.* **52** 385 (1905)
65. A Benrath, G Ritter *J. Prakt. Chem.* **154** 40 (1939)
66. *Gmelins Handbuch der anorganischen Chemie. Kobalt* System-Nr. 58, Teil B, Lfg. 2 (Weinheim: Verlag Chemie, 1966) S. 782
67. *Gmelins Handbuch der anorganischen Chemie. Nikel* System-Nr. 57, Teil B, Lfg. 2 (Weinheim: Verlag Chemie, 1966) S. 1037
68. L V Soboleva *Vyrashchivaine Novykh Funktsional'nykh Monokristallov* (Growth of New Functional Single Crystals) (Moscow: Fizmatlit, 2009)
69. A Pietrashko, Z B Perekalina, L V Soboleva, L F Kirpichnikova *Crystallogr. Rep.* **45** 479 (2000) [*Kristallografiya* **45** 525 (2000)]
70. T H Tahirov, T Lu *Acta Crystallogr., Sect. C* **50** 668 (1994)
71. H Euler, B Barbier, S Klumpp, A Kirfel *Z. Kristallogr.* **215** 473 (2000)
72. A Kirfel, H Klapper, W Schafer *Z. Kristallogr.* **213** 456 (1998)
73. W Kockelmann, W Schafer, A Kirfel, H Klapper, H Euler *Mater. Sci. Forum* **378** – **381** 274 (2001)
74. F Bosi, G Belardi, P Ballirano *Am. Mineral.* **94** 74 (2009)
75. F A Cotton, L M Daniels, C A Murillo, J F Quesada *J. Inorg. Chem.* **32** 4861 (1993)
76. H Montgomery *Acta Crystallogr.* **17** 1478 (1964)
77. E N Maslen, S C Ridout, K J Watson, F H Moore *Acta Crystallogr., Sect. C* **44** 412 (1988)
78. H Euler, B Barbier, A Meents, A Kirfel *Z. Kristallogr.* **218** 409 (2003)
79. E B Rudneva, V L Manomenova, L F Malakhova, A É Voloshin, T N Smirnova *Crystallogr. Rep.* **51** 344 (2006) [*Kristallografiya* **51** 372 (2006)]
80. V L Manomenova, E B Rudneva, L F Malakhova, N G Furmanova, A É Voloshin, T N Smirnova *Crystallogr. Rep.* **52** 918 (2007) [*Kristallografiya* **52** 949 (2007)]
81. R D Shannon *Acta Crystallogr., Sect. A* **32** 751 (1976)
82. E R Nightigale *J. Phys. Chem.* **63** 1381 (1959)
83. X Zhuang, G Su, Y He, Z Guozong *Cryst. Res. Technol.* **41** 1031 (2006)
84. N A Dyatlova, V L Manomenova, A E Voloshin, V V Grebenev, in *Tezisy Dokladov Konferentsii Stran SNG po Rostu Kristallov (RK SNG-2012)* [Abstracts of Reports of the CIS Countries Conference on Crystal Growth (CG CIS-2012), Kharkov, 2012] p. 22
85. X Zhuang, G Su, Y He, Zh Li, G Li, J Ma *J. Cryst. Growth* **244** 359 (2002)
86. L V Soboleva *Inorg. Mater.* **31** 567 (1995) [*Neorg. Mater.* **31** 614 (1995)
87. E B Rudneva, V L Manomenova, A E Voloshin, A B Vasil'ev, in *Tezisy Dokladov XI Natsional'noi Konferentsii po Rostu Kristallov* (Abstracts of Reports of the XIth National Conference on Crystal Growth, Moscow, 2004) p. 283
88. V L Manomenova, E B Rudneva, A E Voloshin, L F Malakhova, in *Book of Abstracts of IUCr 2005, Florence, 2005* p. 438
89. L V Soboleva *Crystallogr. Rep.* **53** 519 (2008) [*Kristallografiya* **53** 555 (2008)]
90. X Wang, X Zhuang, G Su, Y He *J. Opt. Mater.* **31** 233 (2008)
91. V L Manomenova, E B Rudneva, A E Voloshin, E P Kharitonova, A A Lomov, in *Tezisy Dokladov XI Natsional'noi Konferentsii po Rostu Kristallov* (Abstracts of Reports of the XIIIth National Conference on Crystal Growth, Moscow, 2008) p. 246
92. V L Manomenova, E B Rudneva, A E Voloshin, in *Program and Abstract Book of III International Conference 'Crystal Materials 2010', Kharkov, 2010* p. 64
93. V L Manomenova, E B Rudneva, V V Grebenev, M S Lyasnikova, A E Voloshin, in *Tezisy Dokladov Konferentsii Stran SNG po Rostu Kristallov (RK SNG-2012)* [Abstracts of Reports of the CIS Countries Conference on Crystal Growth (CG CIS-2012), Kharkov, 2012] p. 23
94. V L Manomenova, Candidate Thesis in Chemical Sciences, Institute of Crystallography of the Russian Academy of Sciences, Moscow, 2013
95. E P Efremova, V A Kuznetsov, A Yu Klimova, O V Kachalov, I L Smolsky, V S Naumov, M I Kolybaeva, V I Salo *Crystallogr. Rep.* **38** 674 (1993) [*Kristallografiya* **38** 171 (1993)]
96. Patent 2357020 RU (2006)
97. N A Dyatlova, V L Manomenova, E B Rudneva, V V Grebenev, A E Voloshin *Crystallogr. Rep.* **58** 749 (2013) [*Kristallografiya* **58** 737 (2013)]
98. L N Rashkovich *KDP-Family Single Crystals* (Bristol, New York: Adam Hilger, 1991)
99. N R Chaudhuri, G K Pathak *Thermochim. Acta* **12** 71 (1975)
100. X Wang, M Xing *Adv. Mater. Res.* **332** – **334** 1735 (2011)
101. Patent 5788765A US (1998)
102. G Su, X Zhuang, Y He, Z Li, G Wang, G Li, Z Huang *J. Cryst. Growth* **243** 238 (2002)
103. X Zhuang, G Su, G Wang, G Li, Z Huang *Cryst. Res. Technol.* **39** 754 (2004)
104. J M Kavitha, C K Mahadevan *Spectrochim. Acta. Part A* **128** 342 (2014)
105. I Polovinko, S Rikhlyuk, V Koman *Teor. Elektrotekhn.* **60** 163 (2009)
106. V Duraikka, S A Bahadur, S Athimoolam *J. Miner. Mater. Characterizat. Eng.* **11** 1121 (2012)
107. V Masilamani, J Shanthi, V Sheelarani *Crystallogr. Rep.* **59** 1114 (2014)
108. G Su, X Zhuang, Y He, Z Li, G Li, J Ma, G Wang, Z Huang *Cryst. Res. Technol.* **38** 1087 (2003)
109. G Su, X Zhuang, Y He, G Zheng *Opt. Mater.* **30** 916 (2008)
110. N A Vasilyeva, D S Nuzhdin, M A Faddeev, V V Grebenew, V A Lukov, A E Voloshin *Crystallogr. Rep.* **61** 304 (2016) [*Kristallografiya* **61** 306 (2016)]
111. Patent US 20080096097A1 (2008)
112. I I Polovinco, S V Rykhlyuk, V B Koman, I D Karbovnyk *J. Appl. Spectrosc*yu **76** 116 (2009)
113. A E Glikin, S I Kovalev, E B Rudneva, L Yu Kryuchkova, A E Voloshin *J. Cryst. Growth* **255** 150 (2003)
114. A E Voloshin, S I Kovalev, E B Rudneva, A E Glikin *J. Cryst. Growth* **261** 105 (2004)
115. A E Glikin, L Yu Kryuchkova, Yu V Plotkina, N V Taratin *Dokl. Earth Science* **433** 894 (2010) [*Dokl. Akad. Nauk* **433** 85 (2010)]
116. M S Grigoryeva, N A Vasilyeva, V V Artemov, A E Voloshin *Crystallogr. Rep.* **59** 276 (2014) [*Kristallografiya* **59** 316 (2014)]

117. N A Vasilyeva, M S Grigoryeva, V V Grebenev, A E Voloshin *Crystallogr. Rep.* **58** 646 (2013) [*Kristallografiya* **58** 630 (2013)]
118. N A Vasil'eva, N I Sorokina, A M Antipin, I A Verin, A E Voloshin *J. Exp. Theoret. Phys. Lett.* **102** 448 (2015) [*Pis'ma Zh. Eksp. Teoret. Fiz.* **102** 502 (2015)]
119. N A Vasilyeva, N I Sorokina, A M Antipin, I A Verin, A E Voloshin *Crystallogr. Rep.* **61** 11 (2016) [*Kristallografiya* **61** 16 (2016)]